Dinis
Pinto Rosa Bruno

Deposição de nanoestruturas de Au em Si terminado com H baseada em soluções e erosão húmida de bolachas de Si para optoelectrónica

Dinis
Pinto Rosa Bruno

Solution-based deposition of bare Au nanostructures onto H-terminated Si and wet-etching of Si wafers for optoelectronics

o júri

presidente   **Professora Doutora Maria do Rosário Pimenta Correia**
Professora Auxiliar, Universidade de Aveiro

Vogal - Arguente Principal   **Doutor Hugo Manuel Brito Águas**
Professor Associado, Faculdade de Ciências e Tecnologia da Universidade Nova de Lisboa

Vogal - Orientador   **Doutor Rui Nuno Marques Pereira**
Investigador Principal em Regime Laboral, Universidade de Aveiro

Abstract

In this work, we fabricated and studied wet chemically thinned H-terminated silicon substrates decorated with plasmonic AuNPs. The goal of this research was to pursue a deposition method that consistently generated AuNP submonolayer structures on an H-terminated silicon surface. Drop-casting, spin-coating and dip-coating deposition methods of AuNPs on both pristine and thinned silicon substrates were employed and compared. Thinned silicon substrates were produced via wet chemical (KOH) etching to thicknesses down to 50 μm. The AuNPs were produced via pulsed laser ablation in liquid (PLAL) and span in the <50 nm range. The dip-coating method yielded the most consistent and reproducible AuNP submonolayer formations. Both H_2O and THF were used and studied as solvents for the AuNP depositions. THF-based solutions produced spread out and uniform depositions. Dip-coating depositions using a THF-based solution synthesised under PLAL for 90 minutes yielded the highest surface coverage (38%) of all the deposition methods studied.

Palavras-chave

Causticação química, terminação em H, PLAL, nanopartículas de ouro, plasmónica

Resumo

No presente trabalho, fabricamos e estudamos substratos de Si quimicamente causticados com terminação de hidrogénio decorados com nanopartículas de ouro plasmónicas. O objetivo desta investigação é perseguir um método de deposição que crie consistentemente estruturas sub-monocamada de nanopartículas de ouro numa superfície de Si terminada com hidrogénio. Foram empregues e comparados os métodos de *drop-casting*, *spin-coating* e *dip-coating* em substratos de Si não processados e quimicamente causticados. Substratos quimicamente causticados foram produzidos pelo método de ataque químico por KOH, produzindo substratos com espessuras inferiores a 50 μm. As nanopartículas de ouro foram produzidas via *pulsed ablation in liquid* (PLAL) e têm dimensões na gama de <20 nm. O método de *dip-coating* produziu as estruturas sub-monocamada de nanopartículas de ouro mais consistentes e reprodutíveis. H2O e THF foram usados e estudados enquanto solventes para as deposições de nanopartículas de ouro. As deposições por *dip-coating* com THF enquanto solvente sintetizadas por PLAL durante 90 minutos produziram a maior cobertura de superfície (38%) de todos os métodos estudados.

Contents

List of Tables

List of Figures

Chapter 1

Introduction

From optical sensors to solar energy, integrated circuitry and high-end optic elements, silicon is one of the most relevant materials for electronics and optoelectronics applications [1, 2]. In the field of solar energy, thin silicon systems are of great interest due to the reduced diffusion length required for photogenerated electrons and holes to be collected.

The global solar capacity doubled in 3 years from 2018 to 2021, and is expected to more than double again today's output by 2025. It is the fastest growing renewable energy, having had 302 GW of capacity installed internationally in 2021. In Europe, the EU climate goals are propelling the renewable transition, with 25 of the 27 member states projecting to install more solar power in 2022 than in 2021 [3]. Demand for renewable energy sources continually increases due to environmental pollution and resource depletion consequent of use of fossil fuels. Among the various renewable energies, the solar cell technology has been widely adopted due to advantages such as the low maintenance cost and ease of use. One of the largest drawbacks of solar cell technology has been the low energy conversion efficiency arising from optical loss. Thus, numerous studies have been conducted to devise ways to improve solar cell efficiency, with multiple solutions found in recent decades.

There are multiple types of silicon junctions that can be employed for the creation of a functional solar cell. One of these junctions is the Schottky junction. A simple Schottky junction is composed by two components: a metal electrode and a doped semiconductor. It induces charge separation due to the difference between the Fermi level of the metal and the conduction band of the semiconductor, which creates an abrupt potential difference at the junction. Charge carriers traverse this junction through to generate electrical current, as we show in figure 1.1.
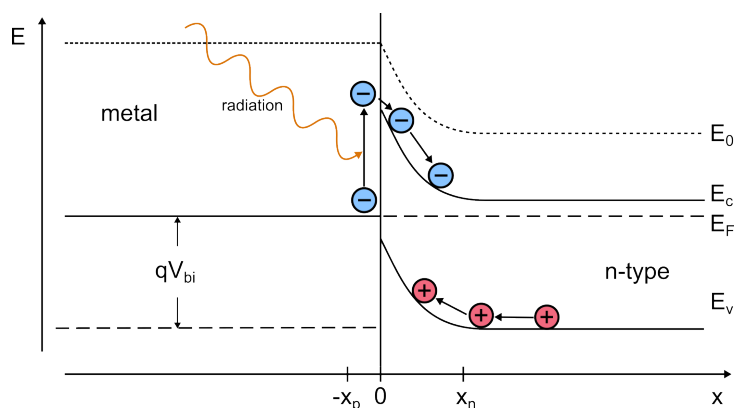
Figure 1.1: Energy bands diagram and charge transport of a Schottky junction under radiation exposure.

Over the last few years, various light-trapping techniques have been implemented in solar

1

cells to increase light absorption within a semiconductor layer that is much smaller compared to the material's absorption length [4, 5]. The optical thickness of an active absorber layer can be increased several times by using light-trapping structures while the physical thickness remains unchanged. This can enhance solar cell efficiency as photo-generated charge carrier collection is improved with little constraints regarding diffusion lengths [6], which allows for thin and efficient solar cells. The most widely used light trapping approaches using nanostructures include periodic grating structures [7], photonic crystal structures [8], nanowires [9, 10], random scattering surfaces [11], and plasmonic structures [12, 13].

The field of plasmonics investigates the interactions between light and metal-dielectric interfaces. It devotes major efforts into the study of coherent electron oscillations triggered by an electromagnetic wave travelling along a metal-dielectric interface. Surface plasmon resonance (SPR) is the interaction between electromagnetic waves and free electrons in metal. There are two modes formed by such electron oscillations. One is the surface plasmon polariton (SPP), which can propagate along the metal-dielectric interface as shown in Figure 1.2. SPPs propagation distance is in sub-centimetre range due to losses deriving from electron scattering [14]. The other one is the localized surface plasmon resonance (LSPR), which is confined in a small
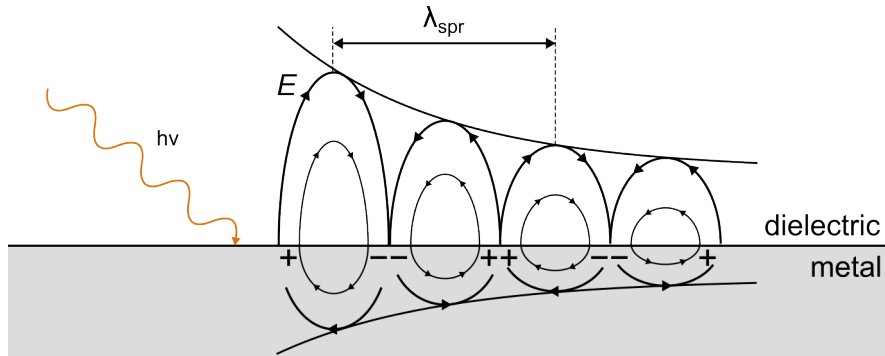
Figure 1.2: Diagram of the propagation of a surface plasmon polariton (SPP) along a metal-dielectric surface.

volume neighbouring a nanoparticle or nanostructure. In figure 1.3, we show the electric field around metal nanoparticles under LSPR. Incident light excites the conduction band electrons of a nanostructure with a size equal or smaller than the incident wavelength generates an LSPR. The frequency at which LSPR occurs strongly depends on the size, geometry, composition, dielectric environment and separation distance of the nanostructures [13, 15]. This phenomenon can remarkably increase the intensity of the electromagnetic field around the metal nanoparticle [16]. Typical applications of plasmonics include bioimaging [17], sensing [18], surface-enhanced Raman scattering [19], chemistry dynamics [20] and photovoltaics [21].

As of today, multiple metal nanostructures with plasmonic enhancement properties have been studied, such as Au [23, 24], Ag [25, 26], Cu [27, 28], through both simulation and experimentation. Similarly, extensive research has been dedicated to the synthesis and deposition of these metal nanostructures on silicon, such as DC sputtering followed by annealing [29, 30], atomic layer deposition [31], nanosphere lithography [32], polyol process [33, 9], transfer printing [34], solid state dewetting [35], pulsed laser ablation in liquid (PLAL) [36, 37], among others. The PLAL method allows for a facile and efficient way of fabricating nanostructures in liquid suspensions, as it does not require vacuum, as well as does not have chemical precursors or functionalization agents that could remain in trace amounts in the dispersion. It allows for the dispersion of bare (non-functionalized) nanoparticles, which is convenient for efficient charge transport across the nanoparticle boundaries. More specifically, gold nanostructures are of great interest for electronic and optoelectronic applications, such as the performance enhancement of ultrathin photovoltaics [30] or the spontaneous emission enhancement via gold nanoantennas
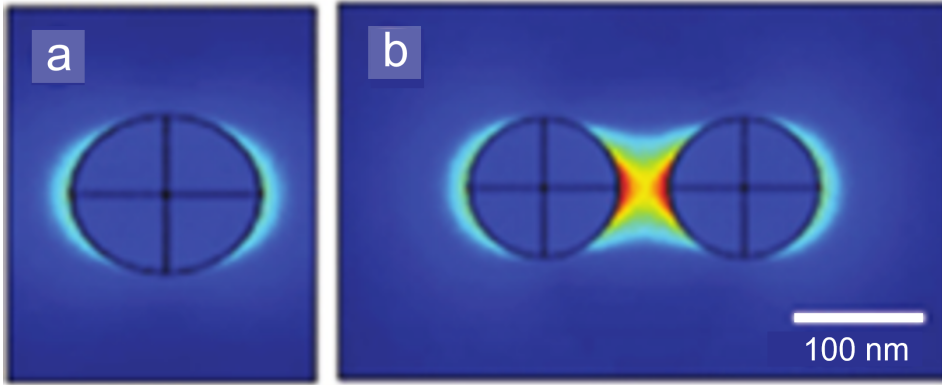
Figure 1.3: (a) Electric field neighbouring a metal nanoparticle under localized surface plasmon resonance (LSPR). (b) Electric field neighbouring two metal nanoparticles under LSPR. Adapted from [22].

[38].

By increasing the absorption via light-trapping and plasmonic methods, it is possible to thin the active layer while maintaining cell efficiency. Methods to thin silicon can be labelled as mechanical or non-mechanical. The most well-established mechanical methods to thin silicon are mechanical grinding [39] and chemical-mechanical polishing (CMP) [40]. Mechanical grinding consists of using one or multiple diamond embedded wheels to remove material from the surface of the target. It has a fast removal rate, but it can create several defects on the surface and subsurface lattice. CMP consists of the same process (grinding with diamond embedded wheels) to remove material from the silicon surface complemented by on-surface chemical treatment. CMP achieves very flat surfaces and low total thickness variation values (TTV) [41]. The most well-established non-mechanical methods to thin silicon are plasma dry etching and wet chemical etching. Plasma dry etching consists of the removal of silicon by the bombardment of ions that subsequently dislodge portions of the material from the exposed surface. Wet chemical etching is based in the removal of silicon atoms from the surface via a chemical reaction between a solution (etchant) and the silicon surface. Both wet chemical and plasma dry etching methods can perform anisotropic etching, that is, etchant attacks preferably a crystal plane with a specific orientation. This property is used for the generation of high aspect ratio nanostructures such as pyramids [42], holes [43] and trenches [44].

In thin silicon structures, the interface has a crucial role in the physics of the device and the defects become increasingly more critical for the energy conversion efficiency, which may be sharply reduced due to large interface recombination losses. The interface recombination velocity, which influences the efficiency of solar cells, is mainly affected by the density and type of interface states. These states result from silicon dangling bonds with different backbond configurations. Passivation methods are used to inhibit unwanted oxide formation and better the performance of the interface. Wet chemical treatments are frequently used to achieve H-terminated silicon, which have better interface electronic properties [45].

In this work, we aim to fabricate and study chemically thinned H-terminated silicon substrates decorated with plasmonic AuNPs. In chapter 1, we covered current synthesis and deposition techniques of metal nanoparticles, followed by an overview on silicon thinning techniques. In chapter 2, we will focus on the experimental techniques we used to fabricate both thinned H-terminated silicon and to synthesize and deposit AuNPs. We will also present the techniques and equipment employed to gather our results. In chapter 3, we will show the results obtained experimentally and subsequently analyse them. We aim to achieve a surface coverage AuNPs that allows for the creation of a percolated mesh. Lastly, in chapter 4 we present the conclusion of our work and address possible approaches and suggestions to be developed in the future.

Chapter 2

Experimental Background

In this chapter, we present the experimental procedures used for both silicon wet etching and gold nanoparticles production. We also approach the methods used for imaging and characterization of our samples.

2.1 KOH etching of silicon

One way of thinning silicon from silicon wafers is to use wet chemical etching. Wet chemical etching consists of the removal or dissolving of material from a substrate when immersed in a liquid etchant solution. The wet etching process can be either isotropic or anisotropic. In an isotropic process, the etchant attacks all crystal planes of the sample similarly, regardless of their orientation. On the contrary, in an anisotropic process, the etchant attacks preferably a crystal plane with a specific orientation. This etchant will ensure that the attack occurs preferentially in a predetermined direction. Since we want to manipulate silicon thickness, while leaving the other dimensions of the sample intact, we want to use an anisotropic etchant. We can achieve this if we choose an etchant with a predominant attack direction to the surface of the wafer. Tetramethylammonium hydroxide (TMAH) [46] and potassium hydroxide (KOH) [47] are frequent picks when it comes to anisotropic etching of silicon. The tetramethylammonium ion is toxic, and when in contact with the human body, it may affect nerves and muscles [48]. Being much safer to manipulate, and with similar results as TMAH, we chose KOH as our etching agent.

When immersed in a strongly aqueous alkaline media such as KOH, crystalline Si can be etched via the following equation,

$$\mathrm{Si} + 2\,\mathrm{OH}^- + 2\,\mathrm{H_2O} \longrightarrow \mathrm{Si(OH)_4} + \mathrm{H_2} \longrightarrow \mathrm{SiO_2(OH)_2}^{2-} + 2\,\mathrm{H_2}$$
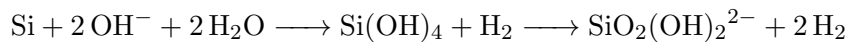
Hydrogen plays an important role in how the etching reaction occurs. As it is produced, it accumulates in tiny bubbles that remain bonded to the surface for a certain period of time. The etch rate of silicon is different regarding the plane which is being etched. The dependence of the etch rate of silicon in KOH on the orientation has been measured at different concentrations and temperatures by Herr [49], Sato [50], Seidel [51], Kendall [52], among others. It has an etch rate anisotropy ratio of about 290:160:1 for [110]:[100]:[111] at 30 wt% and 70 °C[50], changing significantly for other conditions.

Different morphologies arise from etching different planes of silicon after anisotropic etching. The most characteristic feature of Si[100] is the formation of pyramidal hillocks. Pyramids are formed from the top down, in a mechanism where hydrogen bubbles mask the surface and prevent the etching from occurring at the very point of contact. In figure 2.1, we show a diagram representing the pyramid formation process on the surface of silicon. The etching continues around the contact point of the hydrogen bubble, creating four inclined facets with the [111] plane. This four facets form the pyramids typically seen on the etched silicon surface.
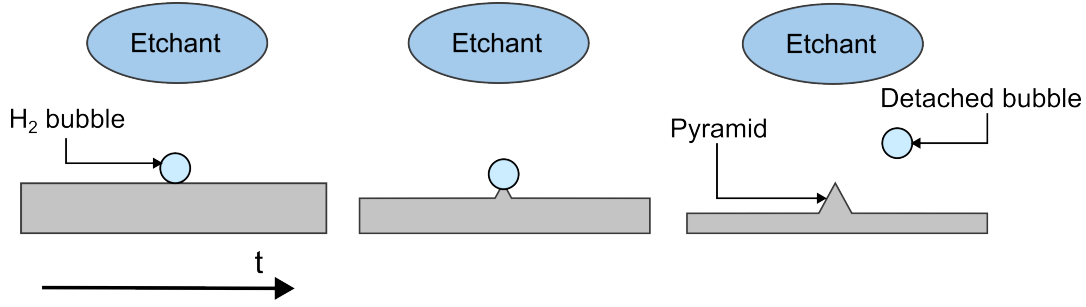
Figure 2.1: Diagram representative of the pyramid formation process by hydrogen bubble masking.

Shallow pits can also be seen in etched [100] silicon. These pyramids can be applied on monocrystalline silicon solar cells for the purpose of light absorption optimization [53]. Etched Si[110] forms channels and perpendicular trenches with {111} side-walls [54], which can be used as e.g. micro-channels in micro-mechanics and micro-fluidics [55].

The etching rate of silicon by KOH is increases with increasing temperature. The surface density of pyramids also increases with increasing temperature. The surface density of pyramids decreases with increasing etchant concentration [56]. Pits can be removed by increasing the concentration of the etchant. Pyramid formation has been also correlated to both water quality and etchant purity [57]. Small concentrations of metal impurities in solution (ppm or even ppb levels) are known to induce pyramid formation [58]. For a chosen concentration and surface orientation, the etch rate R follows an Arrhenius behavior as a function of temperature T

$$R = R_0 \exp\left(\frac{-E_a}{k_B T}\right) \tag{2.1}$$

where $k_B = 8.617 \times 10^{-5}$ eV/K is the Boltzmann's constant, E_a is the activation energy of the atoms on the silicon surface and R_0 is an experimental constant. Based on the reported literature, we set the KOH concentration for the wet silicon etching of the experiments further described to be 20%wt. This concentration provides an etching chemistry that optimizes the silicon etching rate.

Surfactants can be used to improve surface and facets flatness during silicon etching. They prevent the proliferation of hydrogen bubbles, therefore minimizing the masking agents at the surface of the sample [57]. Although not used in our work, isopropyl alcohol is a typical surfactant pick, providing good results at low concentrations. Etching under anodic bias can also improve flatness and suppress the formation of pyramidal structures on the surface of the sample [59].

The combination of wet etching and ultrasonic treatment can significantly improve the etching quality due to the cavitation effect. The formation of cavitation can disable the attachment between H$_2$ bubbles and etching surface, which can promote the reaction between etching solvent and silicon atoms at the surface of the sample. Vibrating of cavitation bubbles can produce high-speed micro jets which promote stirring of the etching solution and reduce temperature inhomogeneity, contributing to a more uniform etching rate [60].

In our work, it is important for the etched silicon substrate to be as flat as possible, in order to replicate the morphology of up and coming devices such as thin silicon solar cells and to promote the formation of percolated AuNP nanostructures on its surface.

2.2   Pulsed laser ablation in liquid

Pulsed laser ablation in liquid (PLAL) is a nanostructure generation method which uses a high-intensity focused pulsed laser beam to extract and ablate nanostructures from a source

material [36]. PLAL is a very efficient and facile way to obtain suspensions and colloids of nanomaterials in multiple solutions. In figure 2.2, we show a schematic representation of a PLAL setup.
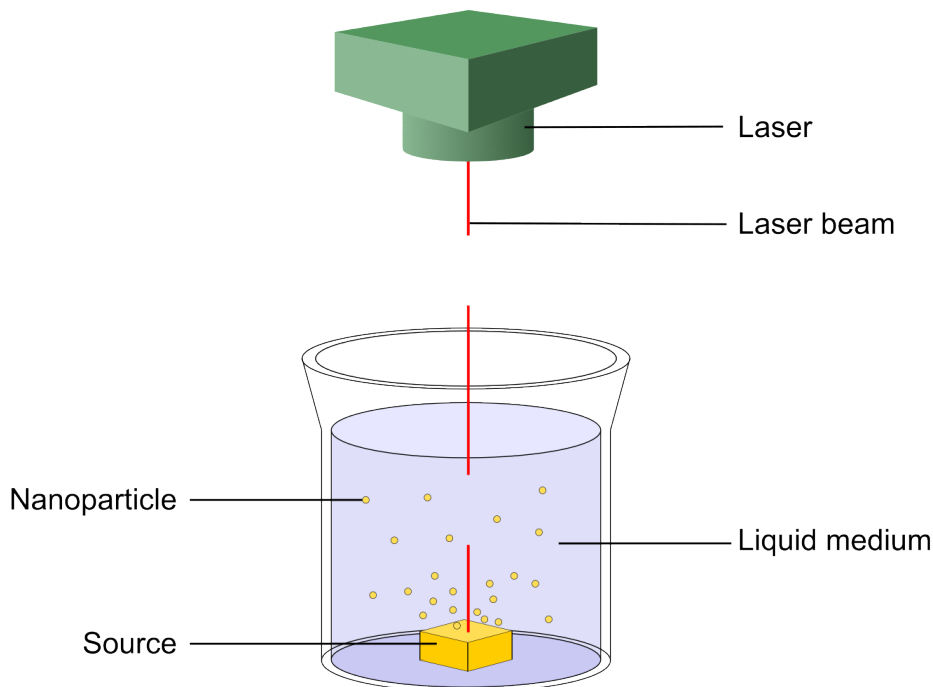
Figure 2.2: Schematic representation of the functioning of an experimental PLAL setup.

In our work, we used PLAL to create gold nanostructure H_2O and THF dispersions from a solid gold target. The system employed in our research consisted of an 1064 nm Nd:YAG laser with a frequency doubler, resulting in an output wavelength λ of 532 nm (green light). The laser is Q-switched, having a frequency f of 10 Hz and a tunable beam length varying between 240 µs and 180 µs.

2.3 Fourier-transform infrared (FTIR) spectroscopy

Fourier-transform infrared spectroscopy (FTIR) employs infrared (IR) radiation to probe the optical properties of molecules in a solid, liquid or gas. This technique acquires an optical interferogram and using a mathematical process known as Fourier transform, it converts the interferogram into an infrared spectrum of absorption, reflection or emission. FTIR is frequently used for the identification of organic, inorganic, and polymeric materials.

In figure 2.3, we show a schematic representation of an FTIR spectrometer. FTIR spectroscopy measurements are obtained in the time domain. This interference pattern obtained is called an interferogram. The interferogram, a time-domain signal, can be converted into the frequency domain via a Fourier transform (FT), yielding the familiar single beam spectrum.

In our work, we used FTIR spectroscopy to measure transmittance spectra of silicon samples treated with KOH. From these spectra, it was possible to extract info regarding sample thickness, as shall be analysed in chapter 3. The system used was a Bruker Vertex 80 FTIR spectrometer [62].
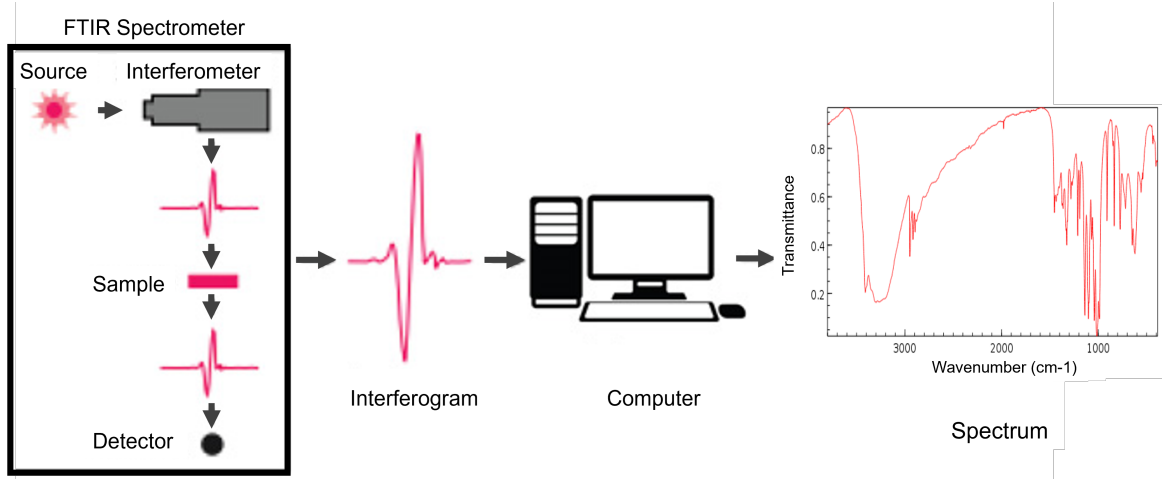
Figure 2.3: Schematic representation of an FTIR spectrometer. Adapted from [61].

2.4 UV-Vis-NIR spectroscopy

UV-Vis-NIR spectroscopy is a powerful technique to determine optical properties such as transmittance, absorbance and reflectance of matter samples. It uses visible light (Vis), ultraviolet (UV) and near-infrared (NIR) light to perform the study of the sample. The visible (Vis) region comprehends the 380-750 nm spectral range. The ultraviolet spectrum (UV) ranges from 10-380 nm although the range typically used in these measurements is 200-380 nm. The near-IR (NIR) ranges from 750-3300 nm. In our studies, the spectral range of the UV-Vis-NIR measurements is 250-900 nm.

UV-Vis-NIR absorbance spectroscopy can be applied on colloidal AuNPs solutions to indirectly calculate the average particle size based on the wavelength position of the maximum of an absorbance band. This absorbance band is related to a surface plasmon resonance (SPR) [63]. These oscillations then propagate parallel to the metal surface. A nanoparticle will absorb most effectively the incoming light with the wavelength matching its resonant peak. The resonant peak wavelength depends on the particle size. Haiss *et al.* obtained a fit that related the diameter (d) with the peak absorbance wavelength (λ_{peak}) of particles with d between 35 and 100 nm, according to the following equation,

$$d = \frac{\ln\left(\dfrac{\lambda_{peak} - \lambda_0}{L_1}\right)}{L_2} \tag{2.2}$$

with $\lambda_0 = 512$ nm, $L_1 = 6.53$ nm and $L_2 = 0.0216$ nm^{-1} being fitting parameters [64]. Later, Khlebtsov *et al.* gathered an extensive amount of experimental data from previous papers, including the one from Haiss *et al.*, and obtained an averaged calibration curve for the diameter of gold nanoparticles (d) as a function their peak absorbance wavelength (λ_{peak}) described by the following equation,

$$d = \begin{cases} 3 + 7.5 \times 10^{-5} X^4, & X < 23 \\ \dfrac{\sqrt{X - 17} - 1}{0.06}, & X \geq 23 \end{cases}, X = \lambda_{peak} - 500 \tag{2.3}$$

where all quantities are expressed in nanometers [65]. This equation should be considered as an empirical generalization of a large volume of experimental data.

In a solid sample, light is scattered and reflected in different ways according to roughness of the surface. High surface roughness typically means a more diffuse reflection, causing a weaker detected signal. UV-Vis-NIR reflectance spectroscopy can be used to qualitatively analyse the

roughness of a sample attacked with KOH through the analysis of its reflectance spectrum and comparing it relatively to the intensity of a pristine and flat sample.

The equipment used for the reflectance studies is a Shimadzu UV-2100PC [66] double beam spectrometer, set up in the range 900-250 nm. The UV-2100PC detects specifically the specular reflection of light.

2.5 Dynamic Light Scattering

Dynamic Light Scattering (DLS) is a rapid and non-invasive technique that measures the Brownian motion of particles in a dispersion for the determination of their hydrodynamic size. The hydrodynamic size, d_h, measured by DLS is defined as the size of a sphere that diffuses at the same rate as the particle being measured. This theoretical sphere is comprised by the core particle complemented by what may be bound to its surface, for example, ions or adsorbed polymers. In a dispersion, the diffusion of particles causes the intensity of light scattered to fluctuate over time.
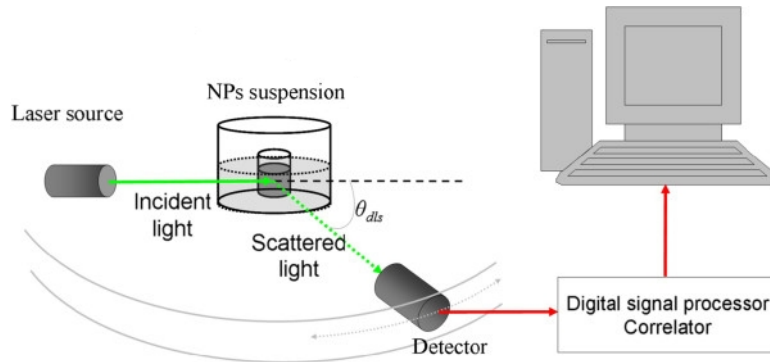
Figure 2.4: Schematic representation of the functioning of a DLS instrument. Adapted from [67].

In figure 2.4, we show a typical DLS measuring setup. A laser beam is pointed towards a sample dispersion that is to be analysed and detected light scattered from the randomly diffusing particles combines to create a speckle pattern. The intensity signal will change over time, as the particles continue to diffuse. DLS analyses the variation of the speckle pattern over time through autocorrelation. The larger the particles being measured, the slower they diffuse, and the longer it takes for a complete loss of the correlation between two distinct signals. For small particles, which undergo rapid diffusion, the correlation of the signal will decay rapidly. The autocorrelation function allows for the extraction of the translational diffusion coefficient, Δ. These are employed in the Stokes-Einstein equation,

$$d_h = \frac{kT}{3\pi\eta\Delta} \tag{2.4}$$

where $k = 1.38 \times 10^{-23}$; j K^{-1}, T is the absolute temperature and η is the viscosity of the solvent. Using DLS, we can quickly measure the size distribution of all particles in a dispersion. Clusters of particles and individual particles are not discerned through the DLS technique, so it is always important to have a critical perspective on the character of the structures measured in suspension.

In our work, it was used the Zetasizer Nano ZS system by Malvern Panalytical [68].

2.6   Scanning electron microscopy

Scanning electron microscopy (SEM) is a technique in which an electron beam is produced and directed towards a sample, producing different types of interactions whose signals are observed by detectors mounted on the microscope at energies typically up do 40 kV. A simple SEM design is composed of an electron gun to emit an electron beam, a set of condenser lens to focus the beam, deflections coils to direct the beam, a sample holder, and a set of detectors to collect the signal resulting from electron-specimen interactions. In figure 2.5, we show a scheme of a simple SEM instrument.
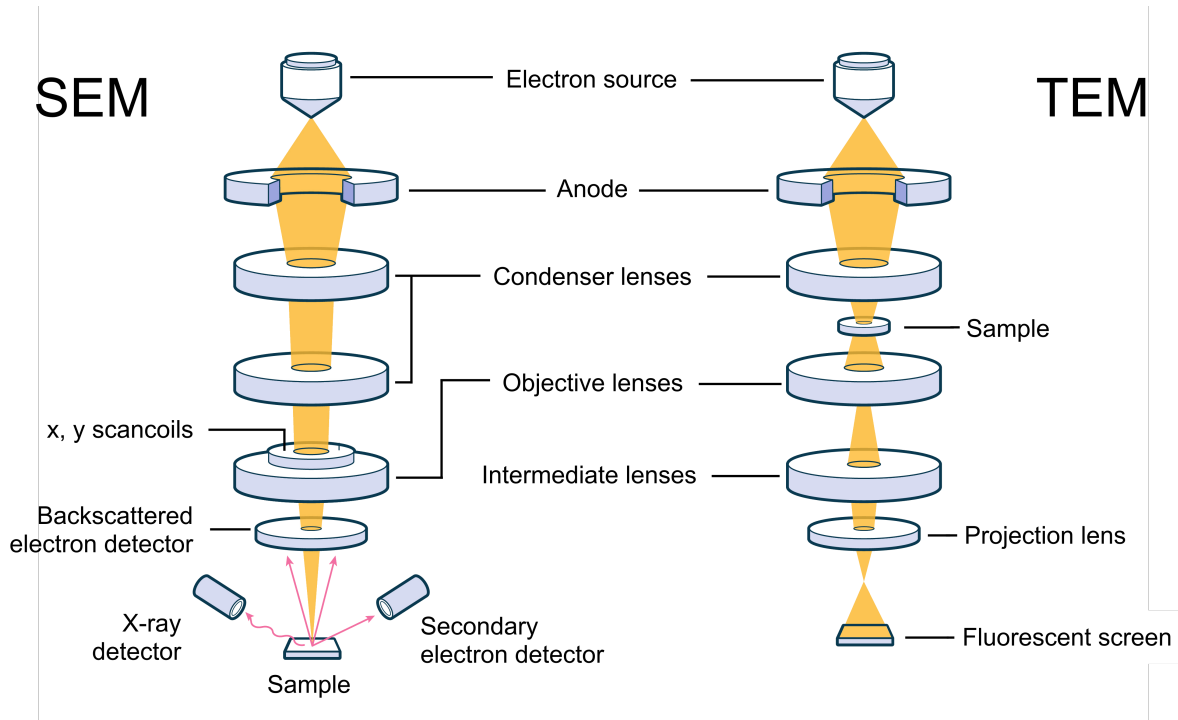
Figure 2.5: Schematic representation of the functioning of SEM and TEM. Adapted from [69].

Secondary electrons, back-scattered electrons and characteristic X-rays are the signals typically collected in an SEM system. Secondary electrons are ejected from conduction or valence bands of the specimen atoms by inelastic scattering interactions with beam electrons. These are typically used to obtain images of the surface morphology of a sample. Back-scattered electrons (BSE) are high-energy electrons that are reflected or back-scattered out of the specimen interaction volume via elastic scattering interactions. Signal collected with BSEs provides better atomic mass contrast when compared to secondary electron signal, although with lower topographic detail. Characteristic X-rays are a consequence of electrons being removed from the inner shell of the atoms by the incoming electron beam. Each atom has its own X-ray signature, thus analysing the characteristic X-ray signal allows the inference of the elements in the sample composition. This technique is commonly referred as energy-dispersive X-ray spectroscopy (EDS), and is used multiple times across the present study to extract information regarding the composition of the samples.

It is fundamental that the sample has conductive properties. In this way, the electrons incoming from the beam flow through the sample and do not accumulate and in this way do not affect the quality of the image acquisition. Making use of the SEM topographic contrast, we employed it for the purpose of analysing the of structure/morphology on the sample's surface. The use of EDS allowed us to analyse the chemical composition of the surface and its distribution. In our work, we used the Tescan VEGA 3 system [70].

2.7 Transmission electron microscopy

Transmission electron microscopy (TEM) is a microscopy technique based on the transmission of highly energetic electrons through a specimen to form an image. The image is formed as a consequence of the interactions of the electron beam with the specimen material. The electron beam source technology and optical system is in many ways similar to that of an SEM. On the other hand, the imaging sensor can be a fluorescent or a sensor such as a scintillator attached to a charge-coupled device. Due to the higher energy of the electrons, and consequently smaller de Broglie wavelength, TEM is capable of imaging at a significantly higher resolution than SEM. In figure 2.5, we show a schematic representation of a typical TEM system.

A particular type of TEM system is the scanning transmission electron microscopy (STEM). Both have similar optics, but while in TEM the electron beam is collimated and hits the sample perpendicularly, in STEM the beam is focused into a small focal point and rasters the surface as the signal is collected. In our work, we used a Hitachi HD-2700 scanning transmission electron microscopy (STEM) [71]. STEM was used to produce high-resolution images of gold nanoparticles in order to assess their size distribution and morphology.

2.8 Atomic force microscopy (AFM)

Atomic force microscopy (AFM) is a high-resolution microscopy that allows to dissect material properties at the nanoscale, with the advantage of easy accessibility to the material and low preparation required. AFM uses a cantilever with a very sharp tip, to the order of nanometers, with which the measurement is made. This tip is brought up close to the sample of interest and allows for imaging of the topography of the sample. For distances greater than 10 nm, the electrostatic and magnetic forces are predominant. The cantilever will be sensible to per-
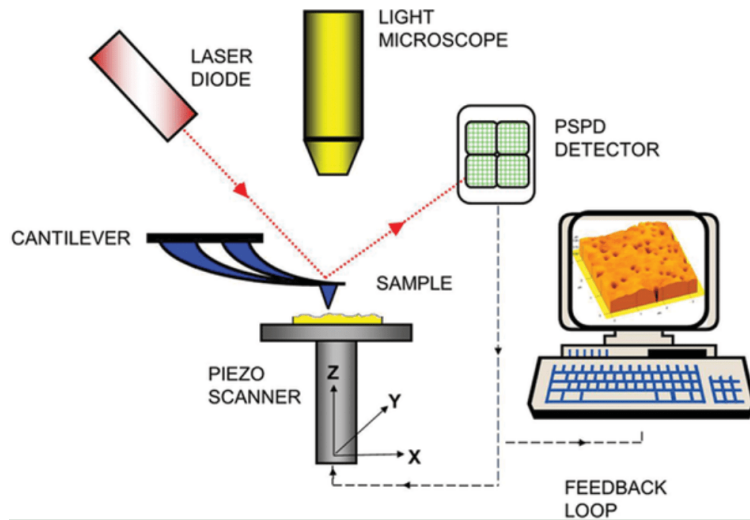
Figure 2.6: Schematic representation of the functioning of AFM. Obtained from [72]

turbations on the surface of the sample. Its movement is measured through the detection of a laser beam which is reflected off the cantilever top. The variations of the deflection angle are tracked by a photodiode and translated into topographic information of the sample. Figure 2.6 represents a scheme of the functioning principle. The imaging method can be one of three types: contact mode, tapping mode and non-contact mode. In non-contact mode, the cantilever oscillates up and down at a reasonable distance from the sample, guaranteeing the preservation of the tip and the sample. Due to the presence of gold nanostructures in the samples studied in the present work, non-contact mode was used for AFM measurements. The software used for AFM analysis is XEI, developed by Park Systems [73].

Chapter 3

Experimental data and discussion

We present and discuss the results of KOH etching of silicon substrates, synthesis of AuNPs suspended in a liquid solution and their deposition onto both pristine and etched silicon substrates.

3.1 Thinning of silicon

In this section, we report the procedures and corresponding results of the thinning of silicon using wet chemical etching with KOH. The etching experiments were carried out with p-type $(5 - 10 \ \Omega \text{cm}^{-1})$ Czochralski-grown Si wafers oriented along [100] direction with a thickness of 279 µm, given by the supplier (Siegert Wafer GmbH). Prior to each etching experiment, each sample went through a thorough cleaning process inside a fumehood. In this, a 1×1 cm sample is subject to a 5 minute acetone ($\geq$99.5%, Honeywell) bath under ultrasonic agitation, followed by an ethanol ($\geq$99.8%, Chem Lab) bath during 5 minutes also under ultrasonic agitation. Subsequently, the sample is immersed in 5% HF to remove the native silicon oxide from the surface, being rinsed with DI water after the treatment. This HF immersion also takes away any fine contaminants that may be resting on the sample surface.

3.1.1 KOH etching cell

At first, a concept was devised that allowed for the predetermination of the area of the sample to be thinned. Here, we used a homemade etching cell that consisted of 2 pieces: a bottom piece, where the sample rests during etching, and a top piece, containing a hole in the center, which is filled with KOH and etches the sample surface [see Figure 3.1(a)]; the top piece is made of Teflon, so that it resists KOH attack. The bottom piece is made of aluminium, due to the high heat conductivity of this material. This is desirable because it will rest over a heat plate (DragonLab MS7-H550-Pro), which will transfer heat to the sample surface and set the etching temperature to a desired value. The temperature of the experiment is measured via a Center 307 Type K thermometer placed inside the bottom piece of the cell, using a small hole (1 mm) drilled below the sample surface. A Viton O-ring is placed in between the top and bottom pieces of the etching cell, so that the KOH is contained and does not leak. It also assures that KOH does not enter in contact with the aluminium (bottom) piece. Figure 3.1(b) shows the schematic representation of the experimental setup.

The temperatures of the sample and of the KOH solution are not the same as the temperature set in the heat plate due to heat loss to the surroundings. Also, the temperature of the KOH solution during etching cannot be easily measured because KOH damages the thermometer. To set a specific temperature on the sample, we must study how the temperature set on the heat plate relates to the temperature of sample. In a series of studies, we related the temperature set at the plate with the temperatures measured at the aluminium piece ther-
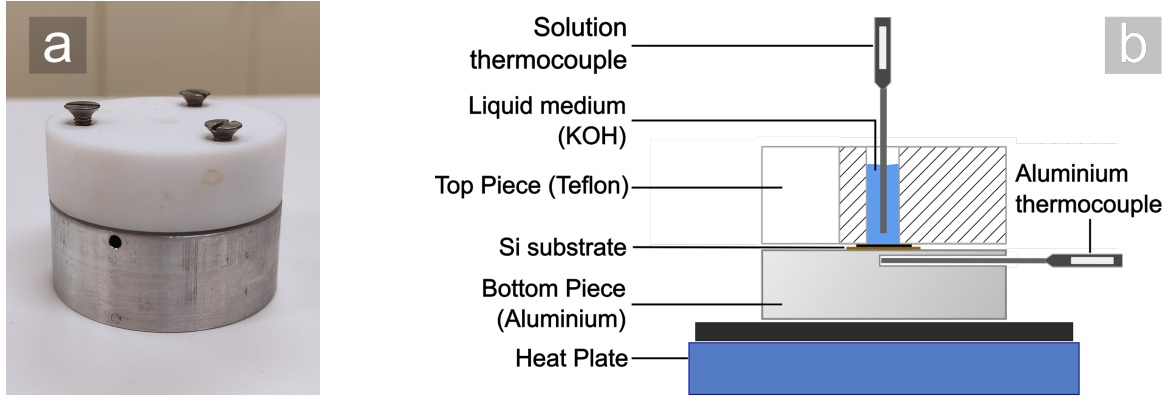
Figure 3.1: (a) Photograph of the homemade etching cell and (b) diagram of the experimental setup using the same etching cell.

mocouple, which we here consider to correspond closely to the silicon sample temperature, and solution thermocouple. The thermocouple in the Al piece is only 0.5 mm away from the silicon substrate.

We started by placing a Si substrate in the etch cell and tightly closing it. The etching cell was empty of any solution. The temperature of the heat plate temperature was set to 70 °C (time $t = 0$ min). At $t = 17$ min, the etch cell was filled with water, as a model system of a KOH solution. Temperature measurements of the aluminium piece T_{Al} and of the water T_{H_2O} inside the etch cell were taken every minute until $t = 31$ min. Figure 3.2(a) shows the temperature evolution of both aforementioned points. As can be seen, the temperature converges to a value of 59 °C and 46 ° for the points under the Si sample and inside the liquid medium, respectively. The asymptotic behavior of the temperature has been estimated by fitting the following equation to the experimental data:

$$T(t) = T_f - \frac{1}{b} \exp\left(\frac{a - t}{b}\right) \tag{3.1}$$

where T is the measured temperature, T_f is the temperature asymptote, a and b are fitting paremeters. In another experiment, we set the temperature of the heat plate to 110 °C and followed the same procedure, with the difference that the empty etch cell was filled with water at $t = 22$ min. In Figure 3.2(b), we show the plot of temperature evolution of both the T_{Al} (i.e. approximately the Si substrate temperature) and T_{H_2O}. As can be seen, the temperatures converge to a value of 87 °C and 74 °, respectively.

For the etching experiments, we aimed for a concentration that would maximize the etching rate. Yun et al. [74] report an etch rate optimal point at roughly 20 wt% KOH. Therefore, we prepared a 20 wt% KOH solution from a 45 wt% KOH solution (Sigma-Aldrich). Then, we aimed for an etching temperature of 80 °C, since it is a good compromise between a fast etch rate and a slow solvent evaporation, and subsequently conducted a KOH etch attack on a Si substrate. The etching lasted 51 minutes, which ended with KOH disposal and rinsing the sample with DI water. After etching, the sample surface was visibly rough, without a mirror-like reflection that it characteristic of a smooth Si surface.

In Figure 3.3(a), we show an SEM image of the surface of the sample (low magnification). The circular silhouette is due to the shape of the Viton O-ring placed on top of the sample during etching and which determines the area of the sample to be etched. Figures 3.3(b), (c) and (d) show SEM images of the surface of the sample recorded at regions 1, 2 and 3 highlighted in Figure 3.3(a). The sample surface has a rough topography and is completely covered with
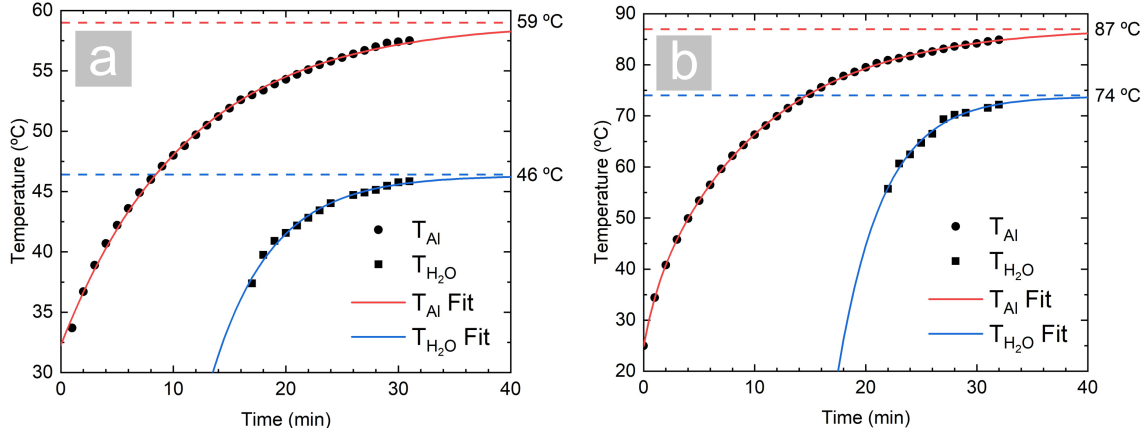
Figure 3.2: Time evolution of the temperatures measured in the Al piece (T_{Al}) and in the liquid medium (T_{H_2O}) for a hot plate set temperature equal to (a) 70 °C and (b) 110 °C. Black symbols are experimental data. The red and blue lines are fits modelled by Equation (3.1).

pyramid-like structures. In Figure 3.4(a), we show an SEM image of the surface zone recorded in Figure 3.3(b) with a higher magnification. Another view of the sample surface is observed in Figure 3.4(b), where we tilted the sample 32.5° over the x axis and recorded an SEM image emphasizing the side profile of the pyramidal structures.

We believe that during etching the hydrogen bubbles that result from the etching chemistry remained on the surface for long periods of time, affecting the etching process. The presence of H_2 bubbles on the Si surface during etching should be a direct consequence of the limited space available inside of the etching cell for these bubbles to easily/quickly escape from the surface. The prolonged presence of H_2 bubbles on the substrate surface prevents the KOH attack on these zones, as is showcased schematically in Figure 2.1, thus leading to a rough surface topology after etching. Due to the high roughness of the surface resulting from etching in the cell, we opted to pursue alternative etching procedures.

3.1.2 Etching by full substrate immersion

As an alternative, we explored the etching by full substrate immersion. This concept was focused on maximizing the flow of KOH solution around the surface of the sample and in this way suppress H_2 bubble masking. For this, we have experimented with etching the Si substrates in KOH solution contained in a large chemistry beaker and in this way maximize the swift exchange of chemical species between the Si surface and the etching solution. In Figure 3.5, we show the experimental setup of etching by full substrate immersion. Here, Si samples were held by a 3D-printed polypropylene (PP) sample holder, chemically inert to KOH, specially manufactured for this process. Other frequent choices for 3D printing, like polylactic acid (PLA) or acrylonitrile butadiene styrene (ABS), were inappropriate due to their weak chemical compatibility with KOH. The designed sample holder had 13 slots (1 mm spacing) that were intended for the samples to fit in vertically. In Figure 3.6(a), we show a photograph the substrate holder piece. Its dimensions are 37.1×50.8×26 mm. This piece was designed to fit in sample of, at least, 10×10 mm in size, as well as 4 inch Si wafers. In order to reduce the masking effect by the substrates holder, the size of the claws that held the samples were minimized and located in places near the border where the samples stand. To improve the flow of KOH solution during etching, the piece contains several holes on its bottom, below the samples.

An issue we had to overcome was that PP has lower density than water (the density of our
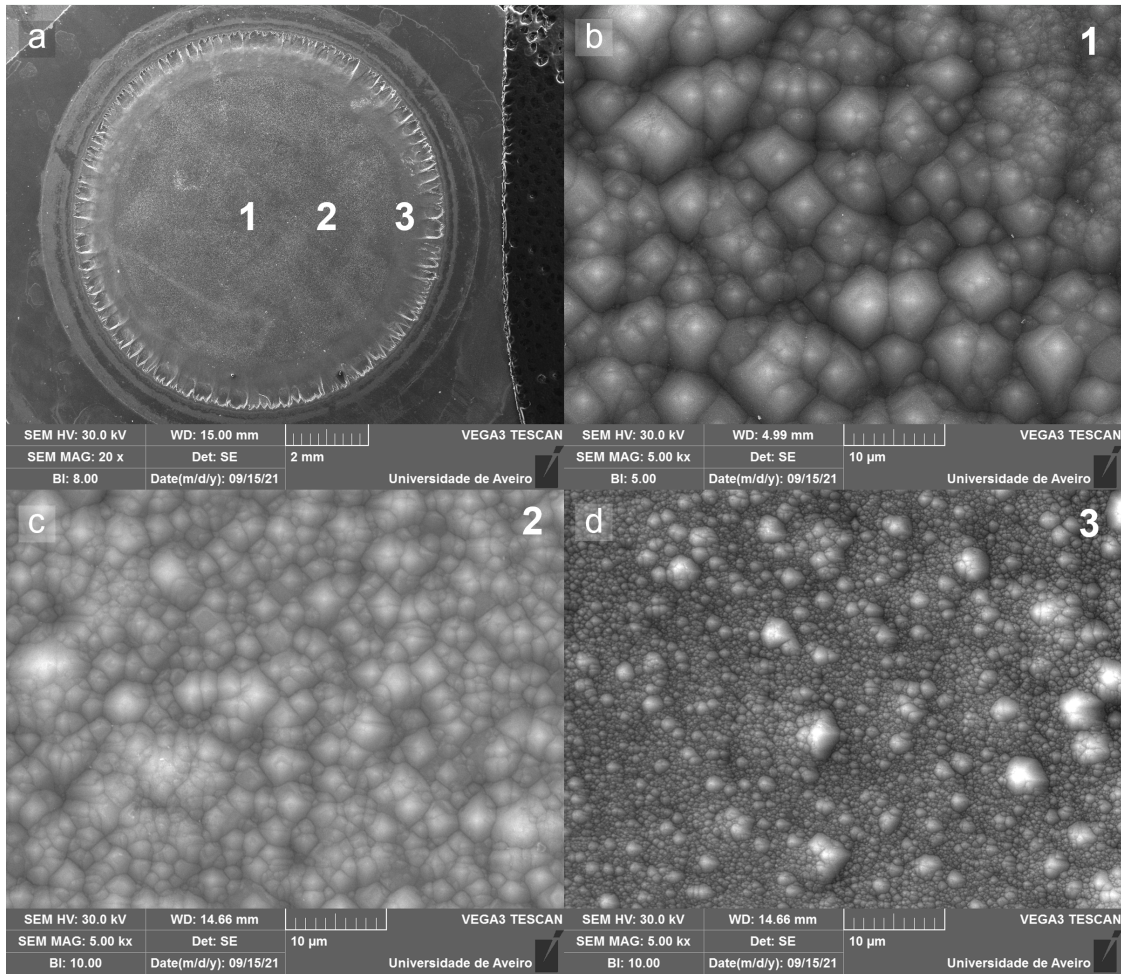
Figure 3.3: SEM images of the sample surface after KOH attack in etching cell recorded (a) at low magnification and (b)-(d) at regions 1, 2 and 3 marked in (a), respectively.
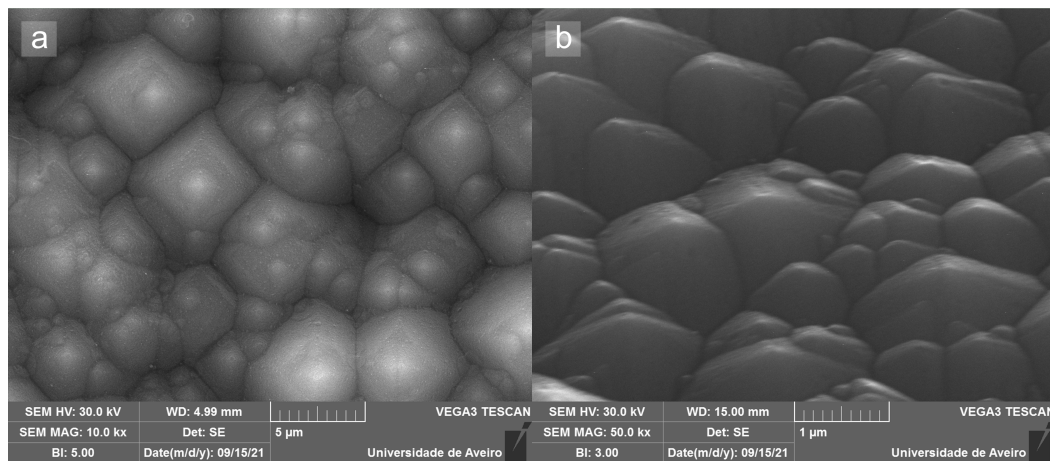
Figure 3.4: SEM images of the sample surface after KOH attack in etching cell recorded (a) perpendicular to the surface and (b) with a 32.5° tilt.

amorphous PP is 0.855 g/cm^3). To overcome this, we designed an auxiliary piece, which function was to press the substrates holder down and not allow it to float. This piece was also made of PP and was held by a laboratory claw during the experiments. A hole was punched in the substrates carrier, where the auxiliary piece would fit in. This concept was successful and was
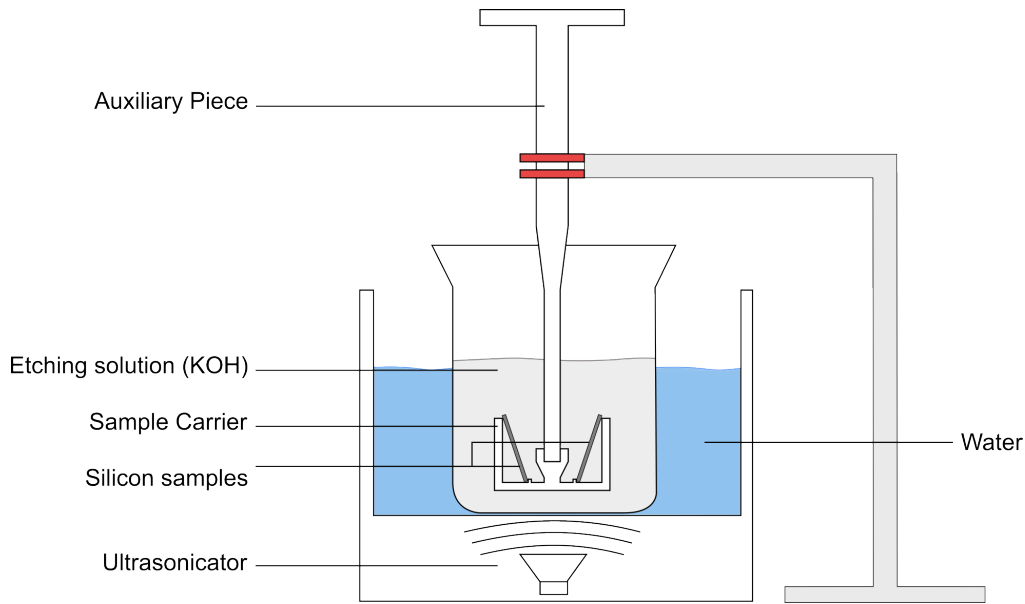
Figure 3.5: Diagram of the experimental setup of etching by full substrate immersion.
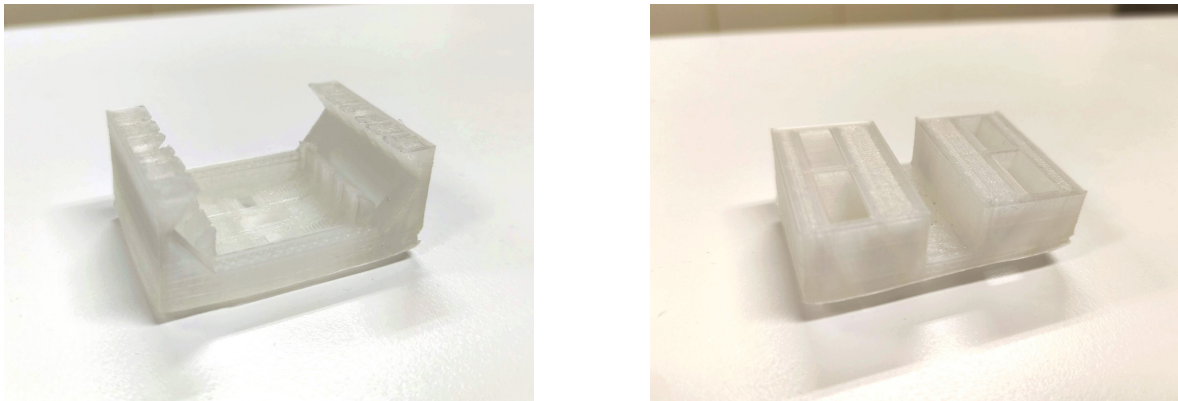
Figure 3.6: Photographs of (a) sample/wafer carrier designed for the KOH etching of Si samples and wafers and (b) sample carrier updated with an ultrasonic resilient design.

adopted throughout the rest of the work. Also, during the first stages of experimenting, samples would become detached from the sample holder due to ultrasonic vibrations. As a result, we updated a more robust design, presented in Figure 3.6(b), that allowed for the simultaneous etch of four 10×10 mm samples.

As shall be described below, we have experimented with performing the KOH etching both without ultrasonic agitation and with ultrasonic agitation. In the latter experiments, ultrasonic agitation was carried out using an ultrasonic bath running at 45 kHz, with an output power of 30 W. In these experiments, the effect of ultrasonic agitation heated the KOH solution. To characterize the temperature at which the KOH etching was effectively carried out, we performed control experiments where we measured the temperature of the ultrasonic bath as a function of time. For this, we recreated the expected experimental conditions. A beaker was filled with approximately 100 mL of water and was placed inside a ultrasonic bath machine, which was in turn filled with roughly 2 cm of water. The temperature was measured with a Delta Ohm HD 2107.1 thermometer placed inside the water inside the beaker. Figure 3.7 shows the measured temperature as a function of time after the ultrasonic machine has been switched on. As can be seen, the temperature raises from the room temperature value to a value close

to 50 °C after about 1 hour. The asymptotic behavior of the temperature has been estimated by fitting Equation (3.1) to the experimental data (t>10 min).
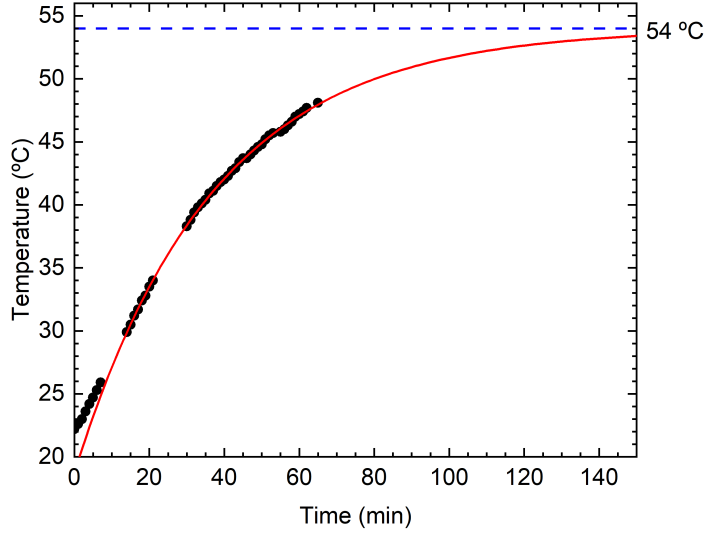
Figure 3.7: Plot of the temperature evolution of the water inside the beaker versus time. Black dots are experimental data points. The red line is a fit using Equation (3.1).

The values of the fit parameters are $T_f = 54$ °C, $a = 264$ °C^{-1} and $b = 37$ °C^{-1}.

Taking into account the heating of the etching solution due to the ultrasonic excitation, we opted to initiate the KOH etching of the samples 60 min after the ultrasonic bath has been switched on. This interim assures sufficient temperature stability of the etching solution during the whole etching. We estimate a temperature of the etching solution in our experiments of $T = 50.5 \pm 3.5$ °C, which corresponds to the temperature interval between temperature measured at $t = 60$ min and the estimated asymptotic value of the temperature $T_f = 54$ °C. To start the etch attack, the sample carrier with the Si substrates is submerged into the etching solution (at $t = 60$ min). In the future, we suggest pre-heating the water before the start of the etching process, as it is a more time efficient procedure.

Effect of ultrasonication. Figure 3.8 shows SEM images of two KOH-etched samples, one etched without ultrasonic agitation (top images) and one etched with ultrasonic agitation (bottom images). Besides ultrasonic agitation, all the other etching conditions were similar: etching duration of 5 hours; KOH solution concentration of 20 wt%. As can be seen in the SEM images, pyramidal structures appear on the silicon surface. In both samples, there are brighter pyramids and dimmer pyramids. The walls of the brighter pyramids face all the same direction. The dimmer pyramid walls present a 45° rotation relatively to the brighter pyramids. The orientation of these pyramids is well defined. The non-agitated sample possesses pyramids with a larger base, compared to the pyramids that appear in the non-agitated sample. Small particles also appear on the samples surface as bright white features in the SEM images. These particles are apparently resting on the surface, not integrating the substrate. They have a higher contrast when compared to the surface, their shape is irregular, they may possess sharp edges and their orientation is arbitrary. We will address and analyse these particles in more detail below.

As mentioned above in Section 2.1, several products yield from the etching reaction of KOH with silicon, namely hydrogen gas (H_2) and dihydroxidodioxidosilicate(2-) [$SiO_2(OH)_2{}^{2-}$]. During etching, hydrogen bubbles are generated on the surface. When a bubble remains on the etched surface, it acts as as a mask and, consequently, the etching reaction is halted at
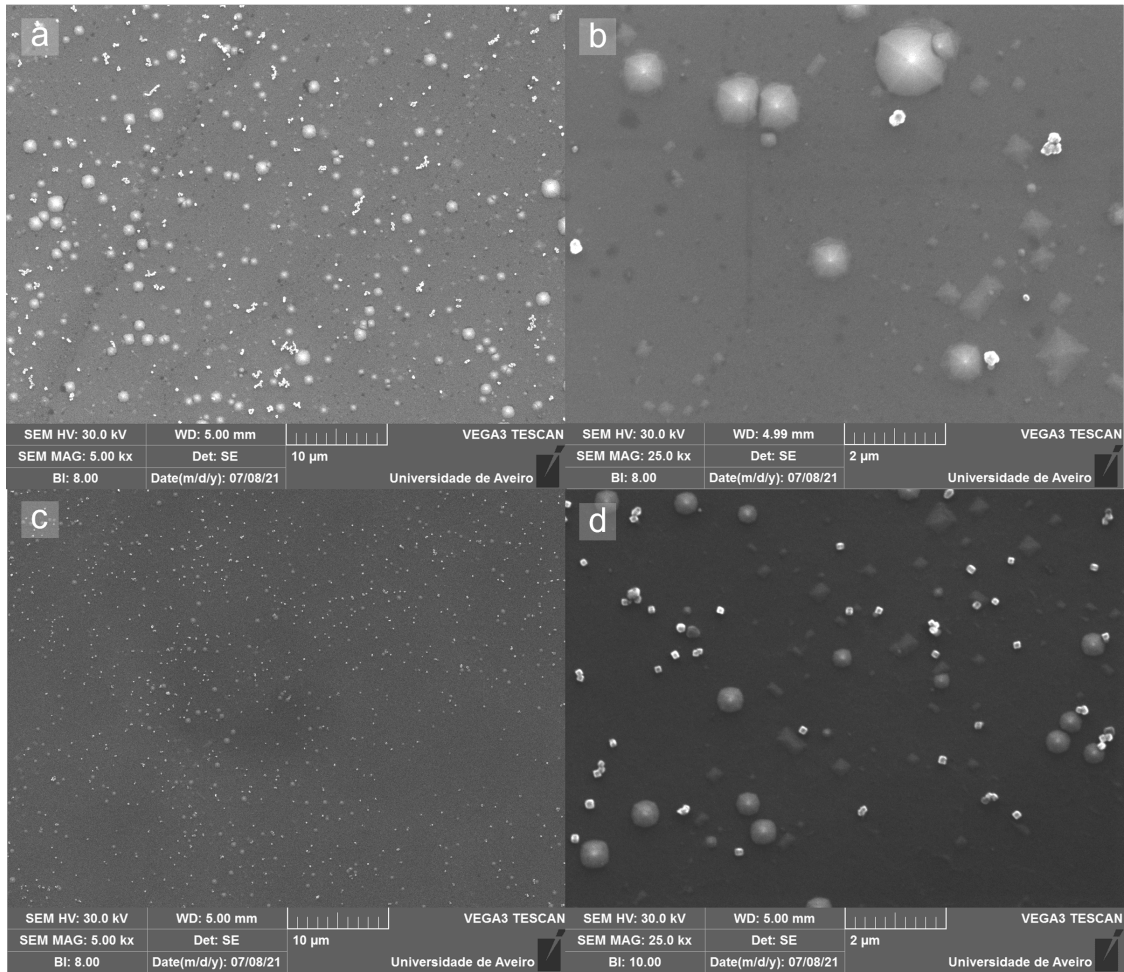
Figure 3.8: (a) and (b) SEM images of a Si substrate sample etched without ultrasonic agitation. (c) and (d) SEM images of a Si substrate etched with ultrasonic agitation.

that point. This phenomenum, repeated many times along the silicon surface, results in the hillocking of the silicon, via the mechanism presented in Figure 2.1. In order to obtain a smooth and uniform silicon surface, these H_2 bubbles must be quickly detached from the surface. By applying ultrasonic agitation, the bubble detachment from the surface is promoted and, consequently, the pyramid formation process is dampened as observed for our samples etched under ultrasonication. KOH etching with ultrasonic bath gave generally better results in terms of smaller size of surface pyramids and consequently a smoother and flatter Si surface. Therefore, we opted to apply this method in the remainder of the work.

We have observed that it is very important to clean thoroughly the sample holder (carrier) before the KOH etching experiments. The cleaning of the sample carrier consisted of an minute acetone bath followed by an ethanol bath, all under ultrasonic agitation. If cleaning is not performed, dirt particles will detach from the sample carrier surface into the solution and mask the surface during etching analogously to H_2 bubble masking, causing the surface of the sample to reveal very large pyramid-like structures which cover most of the substrate.

Effect of etching time. We have analysed the effect of etching time on the thickness of the etched silicon and on their surface morphology. For this, we have carried out a series of experiments where the sample preparation procedures (5 min acetone bath followed by an ethanol bath during 5 min, all under ultrasonic agitation) and etching conditions were the same, varying only the etch duration. For that, we subjected three samples to the same ultrasonically agitated KOH etching bath, for a period of 2, 5 and 7.75 hours.

In Figure 3.9, we show SEM images of the aforementioned three samples. Each row corresponds to a distinct sample. Pyramidal structures are present in all samples. However, the density and size of these pyramids is relatively low, in particular for the samples etched for 2 hours and 7.75 hours. We do not observe any trend on the surface structure morphology as a function of etching time. No trend of an increase or decrease of pyramid size or surface coverage by pyramidal structures is observed against etching duration.
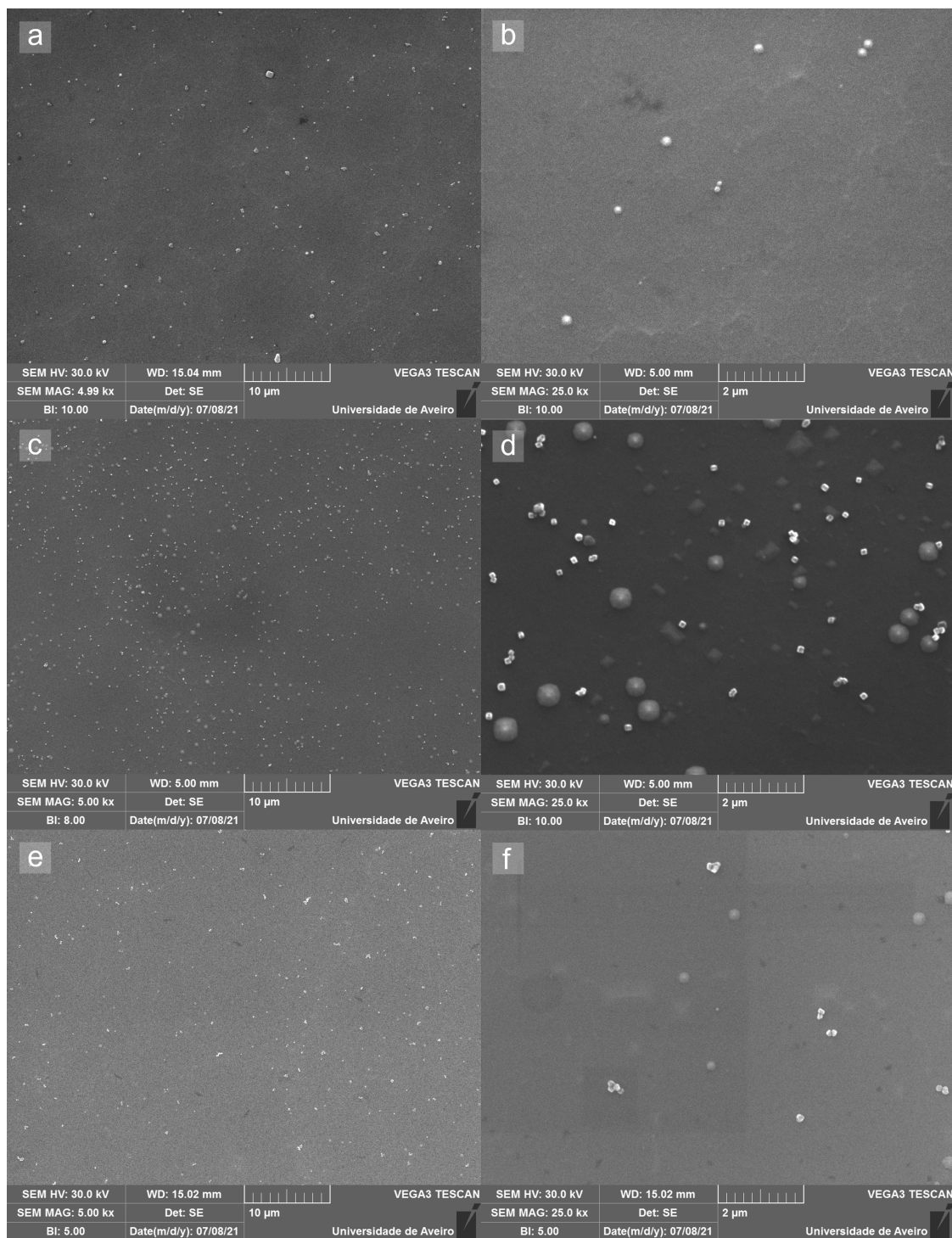
Figure 3.9: Surface morphology of KOH-etched silicon samples during different times of [(a) and (b)] 2 hours, [(c) and (d)] 5 hours and [(e) and (f)] 7.75 hours at ×5K, (f) 7.75 hours at ×25K.

To further infer about the quality of the surface of the KOH-etched samples, and also take conclusions regarding their optical properties, we have carried out studies based on optical reflectance. The reason why we study optical reflectance is that it provides qualitative information regarding the flatness of the surface. The light that hits the surface of the sample either experiences transmission, diffuse reflection or specular reflection. In an etched sample, the roughness of the surface will reduce the specular reflection and promote diffuse reflection. The higher the roughness, the lower the specular reflection intensity and the lower the signal observed at the detector of the spectrometer. Additionally, spectroscopic ellipsometry can be employed in the future as it provides very precise information regarding surface morphology.

In Figure 3.10, we show the (specular) reflectance spectra of six samples. Of these, three are thinned via KOH wet etching and one corresponds to a pristine non-etched silicon reference. For the sake of comparison, we have also included spectra measured for a sample etched using the etching cell (same sample as in Figure 3.3) and measured for a sample etched via the full immersion method and ultrasonication but using a non-cleaned sample carrier. These spectra can be divided into two groups: a group of samples with high reflectance constituted by the three samples and the pristine substrate, and a group of two samples with very low reflectance. The fact that the samples etched with the full immersion method have a reflectivity very similar to that observed for the (reference) pristine silicon samples is indicative of the low roughness of the surface of these samples after etching. These substrates have large areas of the surface not covered by pyramids, as shown by SEM images in Figures 3.9(b), (d) and (e). The other samples are almost completely covered in pyramids, as shown in Figure 3.3. The reflectance on these two samples is very low, especially on the sample that underwent etching in the etching cell, which exhibited pyramids and other structures all over its surface (Figure 3.3). Also, we can see that a 1-hour etched sample under ultrasonic agitation presented high roughness, a consequence of using an uncleaned sample holder. This issue which was overcome in the following trials by thoroughly cleaning the sample carrier.
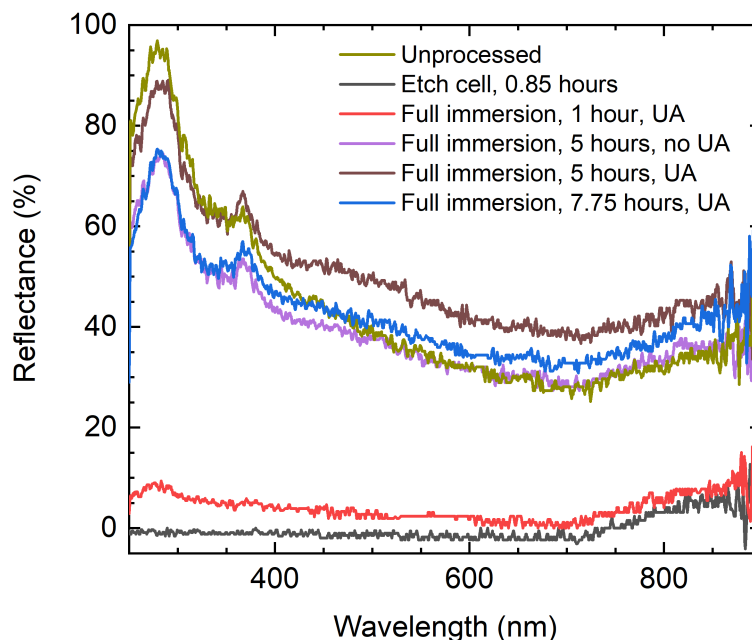
Figure 3.10: Reflectance spectra recorded for KOH-etched samples and one pristine Si sample.

There are several techniques to measure the thickness of thin materials, based in optical phenomena (ellipsometry, optical interference), contact probing (atomic force microscopy, profilometry), high-energy particle scattering (scanning electron microscopy, Rutherford back-

scattering), among others. To obtain the thickness of the thinned silicon samples, we propose and employ the technique of optical interference. This technique requires the sample to be flat, in order to prevent light scattering that will restrict the interference effect. Moreover, both the front and back surfaces of the sample must be parallel (as in Fabry-Perot interferometry). Advantages of this method are that it is quick and non-invasive. A drawback of this method is that it is not very effective in high-roughness samples. When analysing the FTIR transmittance spectra of thin and flat samples, fringes appear due to the interference between the optic beam reflected in the front and back boundaries of the sample and optic beam that directly traverses the sample. The interferometry technique is based on the analysis of the wavenumber difference between fringes in the optical spectra. Thinner samples originate fringes with more spaced maxima. This spacing is then used to calculate the distance between the two planes on which the light beam is reflected off. Since the interference planes correspond to both boundaries of our sample of study, the distance between them corresponds to the sample thickness. Being an apolar and covalent material, silicon does not present an FTIR signature. However, it is possibe to observe absorbance peaks in the sub-2000 cm^{-1} range. Although they were not on the scope of our research, the chemical nature of the compounds originating these absorbance peaks can be the subject of a future work.
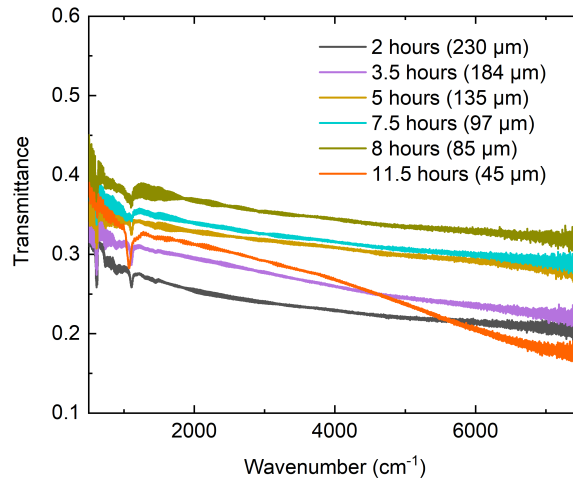
Figure 3.11: FTIR spectra of KOH-etched silicon samples during different times. Values in parenthesis correspond to sample thicknesses obtained from optical interferometry.

In Figure 3.11, we show FTIR spectra of six (distinct from the previously mentioned) samples etched in KOH for different durations. As can be seen, the transmittance of the samples increases with etching time, which is consistent with the Beer-Lambert law. However, at the highest etching time (11.5 hours), the transmittance drops significantly, being this drop more pronounced in the NIR region. This is indicative that, at this etching time, the surface roughness is increased, promoting diffuse light scattering and consequently curtailing the transmittance of non-scattered light.

In Figure 3.12 we show sections of FTIR spectra measured for three samples etched during three different times which show interference patterns. We highlight two maxima of the interference fringes of one of the spectra. The thickness z of the Si samples can be obtained from the position of consecutive maxima from

$$z = \frac{1}{2n(\nu_2 - \nu_1)} \tag{3.2}$$

where n is the refractive index of silicon, which we set to 3.415, corresponding to the value reported for 293 K at 1000 cm^{-1} [75], and ν_1 and ν_2 are two adjacent interference maxima (indicated in Figure 3.12). Knowing the thickness of the original silicon l (279 μm) and the
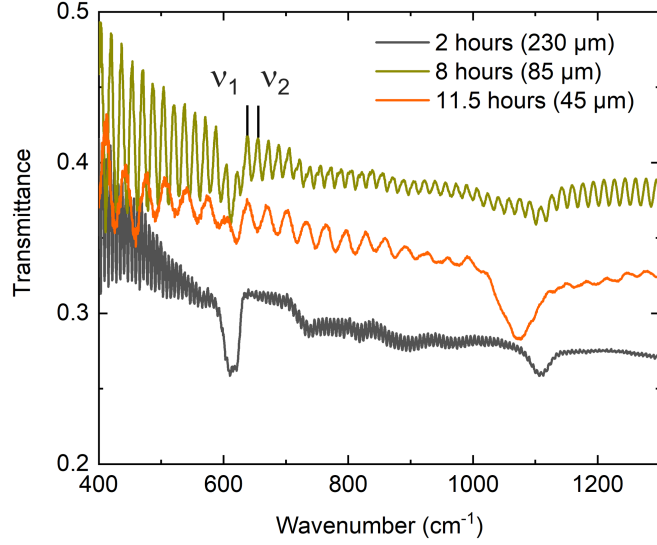
Figure 3.12: FTIR spectra of samples KOH-etched for different times and correspondingly having different thicknesses.

thickness of the etched silicon z, the etch depth is

$$D = l - z \tag{3.3}$$

Considering that the etch rate slightly varies over time due to reagent consumption and product saturation, and taking into account that the etching depth D is expected to be 0 μm for an etching time $t = 0$ s, we model the etching process as

$$D = \xi_0 t + \frac{a}{2} t^2 \tag{3.4}$$

where ξ_0 is the etch rate at $t = 0$ h and a is etch rate variation over time.

Figure 3.13 shows data corresponding to the etch depth against etch duration of all samples analysed and the respective quadratic regression with Equation (3.4).

The regression has an initial slope ξ_0 of 36 μm/h, and an 8-hour average etch rate of 25.4
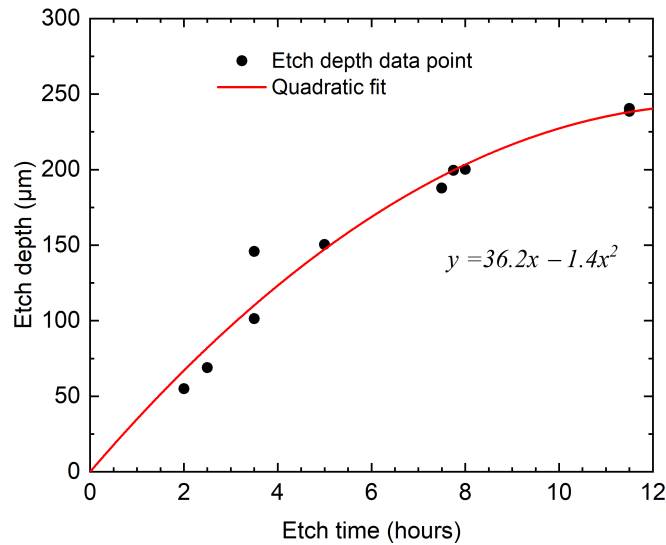
Figure 3.13: Etch depth observed for Si samples against etch time.

21

μm/h, which corresponds to an etch rate of $\xi = 0.42$ μm/min. Other etching rates obtained in literature are 0.36 μm/min reported for $T = 50$ °C 20%KOH etch without ultrasonic agitation in [76] or a 0.45 μm/min reported for a 60°C 20%KOH etch with ultrasonic agitation in [51]. Both studies used profilometry to measure the etch depth D. Our experimental etching rate follows closely the etching rate values reported in these past experiments.

Surface contaminants. The presence of microparticles on the surface of our KOH-etched samples, observed in SEM images shown above (Figures 3.9 and 3.14) is unexpected, thus we analyzed these particles in greater detail. Figure 3.14(a) shows an SEM image of the surface of the silicon sample etched for 5 hours with ultrasonic agitation. In this figure, it is noticeable the emergence of two types of structures on the surface: dimmer structures with a bright point in the middle and brighter and less regular particles. As we will confirm below, the dimmer structures are pyramids consequent of the etching process, while the brighter structures are contaminant particles. In order to understand the nature of these particles and ultimately remove them, we must study their composition. For this, a multipoint EDS analysis was performed, as shown in Figure 3.14(b). For Point 1 and Point 2, we targeted two bright particles. The EDS spectra yielded a peak pattern corresponding to Fe, as we can see in Figure 3.14(c). For Point 3, we targeted a dimmer structure on the surface of the substrate and it showed a single Si peak on its EDS pattern, confirming that this structure is a pyramid exclusively composed of silicon. The source of the Fe in the samples was a rusty lab claw.
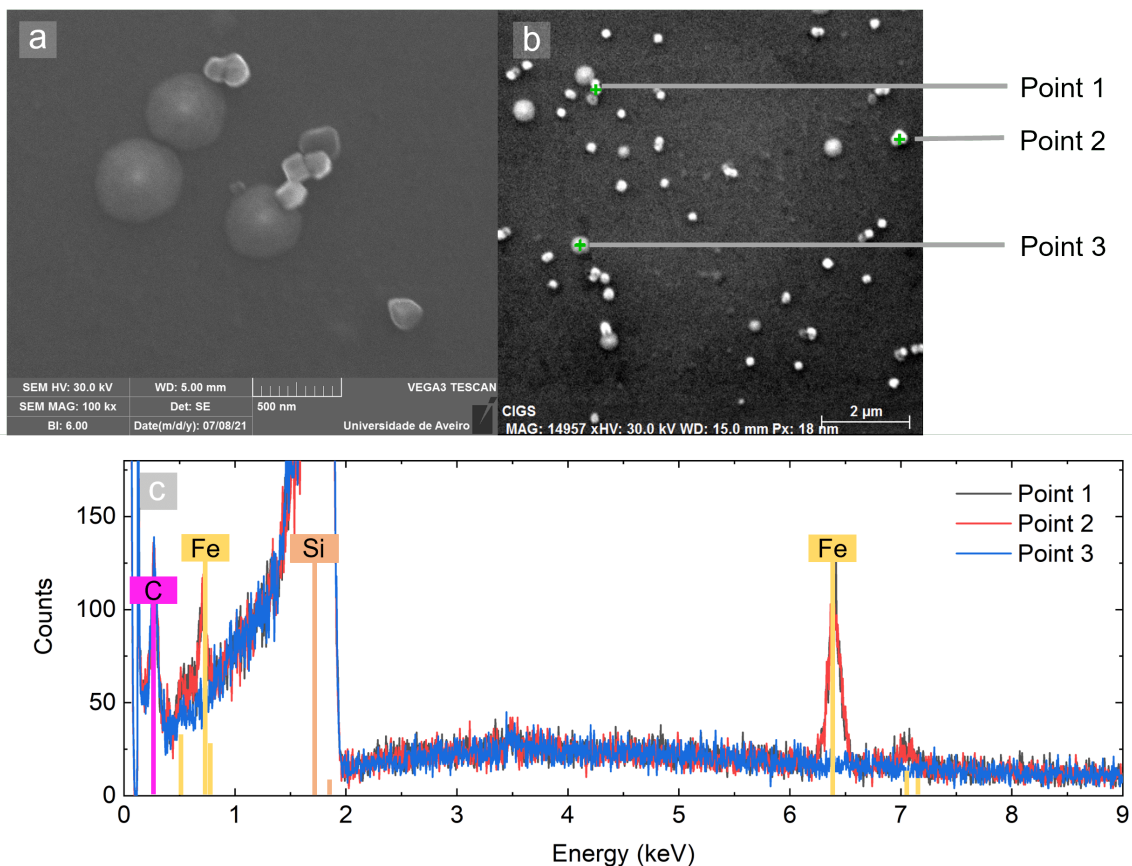
Figure 3.14: (a) High magnification SEM image of a 5-hour-etched sample. (b) SEM image of the same sample highlighting 3 points where EDS was performed. (c) EDS spectra corresponding to the points highlighted in (b).

Once we have obtained the composition of the contaminant particles on the KOH-etched samples, we set towards the engineering of treatments to remove these particles, without modifying the surface morphology. We considered two different processes as candidates to cleaning.

One candidate consisted of simply subjecting the sample to acetone (5 minutes) and alcohol (5 minutes) baths under ultrasonic agitation. Although this is a standard treatment to clean Si substrates, this treatment was not effective to remove Fe particles. The other candidate for removing the Fe particles was a method that had the same basis steps as the above one (acetone and alcohol baths with ultrasonication), with an additional final step, consisting of an HF etching for 5 minutes. Hydrofluoric acid is a substance that strongly attacks metals like Fe while should preserve the underlying Si surface structure, due to a slower etch rate of silicon [77]. In Figure 3.15, we show SEM images the surface of a KOH-etched Si samples recorded before (contamined) and after (cleaned) being subject to the Fe microparticle removal procedure. After the treatment, the presence of Fe particles was considerably reduced and, if rarely present, had a smaller size relatively to the pre-treated sample. The reduced size of these particles suggests that with a few more minutes of HF etching, these particles would completely disappear. Therefore, this procedure should be adopted to remove any trace contamination of Fe origin.
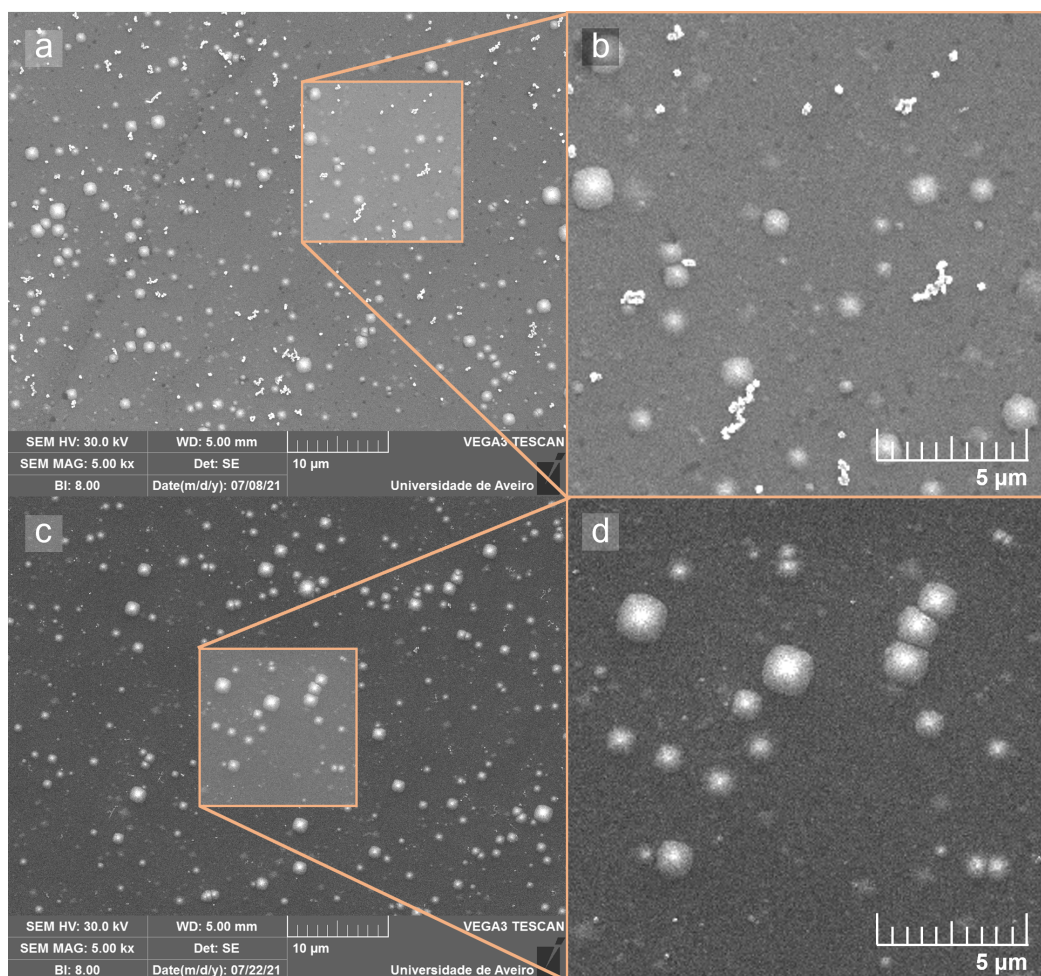
Figure 3.15: (a) and (b) SEM images of KOH-etched silicon with Fe microparticles at the surface. (c) and (d) SEM images of the same sample after acetone and alcohol treatment under ultrasonic bath, followed by HF dipping.

3.2 Au nanoparticles synthesis and deposition

Another part of this work consisted in the synthesis and deposition of gold nanoparticles (AuNPs) on a H-terminated silicon surface. In this way, metal-semiconductor nanointerfaces are assembled with potentially plasmonic properties on the silicon-gold boundary.

In this Section, we will firstly focus on the method of fabrication of the AuNPs. We employed pulsed laser ablation in liquid (PLAL) in two distinct solvents: water and tetrahydrofuran (THF). Then, we will study the depositions onto H-terminated silicon of the resulting AuNP solutions by means of drop-casting, spin-coating and dip-coating. The results of the depositions are analysed through of SEM, TEM, AFM and optical spectroscopy.

3.2.1 Synthesis of Au nanoparticles

Here, we used pulsed laser ablation in liquid (PLAL). This method consists in the emission of short and intense laser pulses directed towards a target immersed in a liquid. The short and intense laser pulses eject material from the target surface, releasing particles from the target into the liquid medium [36]. The particle size can vary upon duration of the beam, intensity of the beam and type of liquid medium (water and THF). In our case, the target was a pure solid Au disk. To disperse AuNPs in organic solvents (like THF), the AuNPs are frequently surface functionalized, meaning that an organic molecule (e.g. a thiol) is covalently grafted to the surface [78]. This functionalization results directly from the synthesis of the AuNPs using chemical routes or may be added after synthesis using wet chemistry [79].

We chose the PLAL because it enables the production of dispersions of bare (non-functionalized) AuNPs in organic solvents that can be used to deposit AuNPs onto H-terminated Si surfaces using solution processing methods. An advantage of PLAL is its effectiveness to consistently generate Au particles with nanoscale size. This method of synthesis does not require any chemical precursors to generate the AuNPs. This means that the solution is free of trace elements deriving from the process of synthesising the AuNPs. However, when dissolved in H_2O, AuNPs attract each other and aggregate into large clusters, inconvenient to our purpose. Various methods have been developed to overcome AuNP aggregation [80, 81]. In our work, the H_2O solution was stabilized with KCl at a concentration of 0.1 mM.

To generate the AuNPs suspended in a solvent, we started by placing the gold target at the bottom of the beaker. We filled the beaker with the solvent in which the AuNPs would be dispersed (H_2O or THF) to a height of about 20 mm. The gold target is then fully submerged by the solvent and the beaker is placed in the optical path of a high-intensity laser beam. The position of the beaker is such that the laser beam hits directly the gold target. Once the setup is complete, the laser is turned on, starting the ablation of the gold target. In Table 3.1, we show the synthesis conditions of all solutions used in our work. Once the synthesis time is reached, the laser is turned off and the beaker containing the AuNPs solution is removed from the optical path. The solution is then transferred to small storage containers for further experimenting. The synthesis parameters of all AuNP dispersions produced and studied within this work are summarized in Table 3.1. In Figure 3.16(a) and (b), we show H_2O- and THF-based AuNPs solutions stored in small beakers, respectively.

In Figure 3.17, we show the absorbance spectra of all six distinct AuNP dispersions. The data are labelled according to Table 3.1 labels. All absorbance spectra show a peak in the 500-550 nm region, which corresponds to the SPR of the AuNPs in the dispersions. The wavelength of this peak (λ_{SPR}) can be used to obtain information about the mean size of the AuNPs according to the relation shown in Equation (2.3). The values of λ_{SPR} observed for each solution are summarized in Table 2. Solution A has an SPR peak at 503 nm, assigned to NPs around 10 nm in diameter. Solution B has a SPR peak at 515 nm, assigned to NPs of around 15-20 nm, but a shoulder is observed in the optical spectrum, which indicates some aggregation. Solutions C,

	A	**B**	**C**	**D**	**E**	**F**
Liquid medium	H$_2$O	THF	THF	THF	THF	THF
Laser parameters						
λ (nm)	532	532	532	532	532	532
f (Hz)	10	10	10	10	10	10
Volume (mL)	40	40	40	40	40	40
Liquid column height (mm)	∼20	∼20	∼20	∼20	∼20	∼20
Q-switch (μs)	240	240	240	210	180	180
Synthesis time (min)	30	30	30	30	30	90

Table 3.1: Summary of the synthesis conditions of all AuNP dispersions produced.
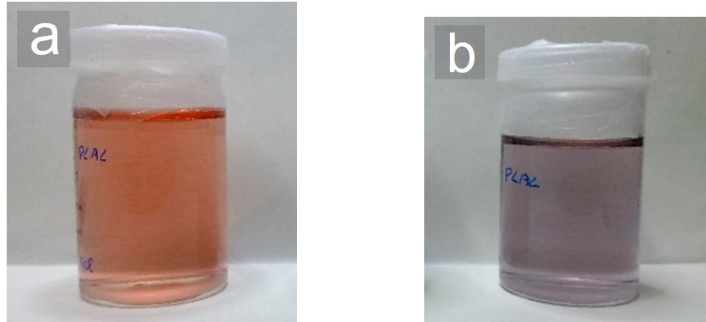
Figure 3.16: Photographs of solutions (a) *A* and (b) *B*.

D, *E* and *F* have peaks ranging from 531 nm and 536 nm, as we can see in Table 3.2, assigned to NPs around 45-60 nm.

To measure sizes of the dispersed AuNPs, another technique used was dynamic light scattering (DLS). A particularity of DLS is that it does not differentiate clusters of AuNPs from isolated NPs. This means that frequently DLS reports a multimodal distribution of sizes of particles due to the presence of clustered NPs. The average sizes and corresponding representativity obtained for all the solutions *A-F* are summarized in Table 3.3. In solutions *A*, *B*, *C* and *F*, DLS reveals an average particle hydrodynamic diameter of 6 nm, 121 nm, 94 nm and 32 nm, respectively. Solutions *D* and *E* reveal bimodal distributions. In solution *D*, DLS reveals two peaks, corresponding to particle sizes of 49 nm and 97 nm. The 97 nm peak has a representativity of 77%, which suggests that in this solution the AuNPs are mostly clustered into larger structures. In solution *E*, DLS reveals two peaks, corresponding to particle (or cluster) sizes of 31 nm and 72 nm with similar representativity.

In order to have a precise and visual representation of the AuNPs size deposited on the silicon substrate, STEM measurements were carried out. We studied the AuNPs size distribution of solutions *C*, *D*, *E* and *F* via several STEM measurements. At the time of the STEM measurements, as we will see further ahead in the present document, we had already chosen THF as our main solvent for the AuNP dispersions, and for that reason, solution *A* was not studied through the scope of STEM. In Figure 3.20, we show the distribution of the AuNP diameters obtained from STEM images. We applied a lognormal curve to fit the obtained data. The STEM results show that the average AuNP size is approximately 10 nm. The size of the AuNPs remains constant and seems independent of the Q-switch or synthesis time. By comparing these STEM results with those obtained through DLS, we infer that the AuNPs agglomerate into (>30 nm) clusters when suspended in THF.
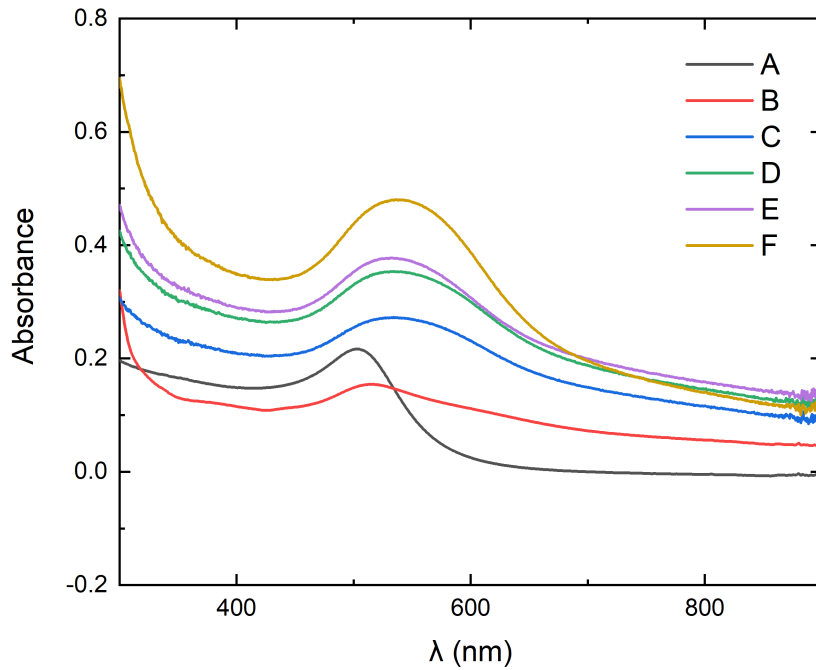
Figure 3.17: Absorption spectra of solutions *A* to *F*.

	A	*B*	*C*	*D*	*E*	*F*
$\lambda_{\mathbf{SPR}}$ **(nm)**	503	515	535	535	531	537
Mean diameter (nm)	3	7	53	53	46	57

Table 3.2: Absorbance peak wavelengths and corresponding particle mean diameter (using Equation (2.3)) of each solution produced in our work.
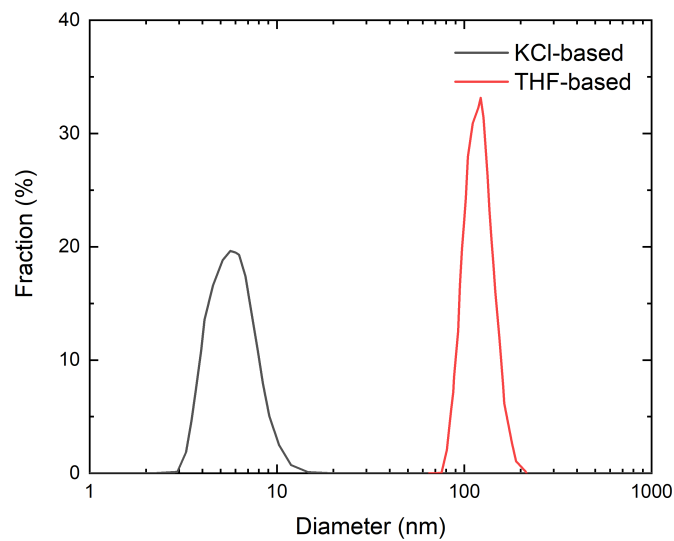
Figure 3.18: Plot of the AuNPs size distribution of solutions *A* and *B*.

	A	B	C	D		E		F
				Peak 1	Peak 2	Peak 1	Peak 2	
Mean diameter (nm)	6.0	121.3	94.1	49.7	97.2	31.4	72.3	32.2
Fraction	1	1	1	0.23	0.77	0.55	0.45	1

Table 3.3: Average particle diameters and corresponding representativity with the use of DLS results from solutions A to F.

Figure 3.19: STEM image of AuNPs deposited from a THF-based solution, highlighting their perimeters.
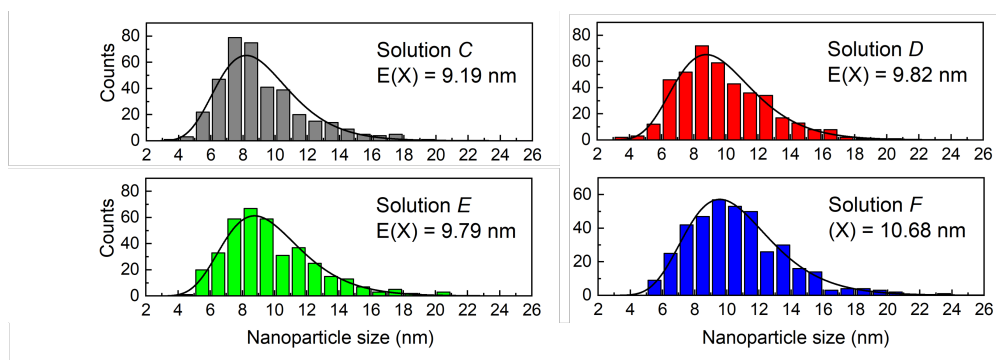
Figure 3.20: Distribution of diameters of AuNPs obtained from STEM images.

3.2.2 Solution-based deposition of Au nanostructures

Deposition from H₂O- and THF-based solutions: drop-casting and spin-coating

In Figure 3.21(a)-(d), we show SEM images of a silicon substrate after AuNP deposition via drop-casting a solution of AuNPs in H_2O (solution *A* of Table 1). The silicon substrate the standard cleaning procedure described in the beginning of the present chapter. Then, a 120 μL droplet of solution *A* was dropped onto the sample surface. The solution was let to rest until it was completely evaporated over the course of roughly one hour. As can be seen from the images of Figure 3.21(a)-(d). We observe that the deposition of AuNPs is not uniform. The coverage of the surface with AuNPs in Figures 3.21(a) and (d) is relatively high, corresponding to a fraction of 44% and 66% of the total substrate area. In Figure 3.21(b) and (c), the surface coverage is nearly negligible, with only very few nanoparticles.

In Figure 3.21(d1)-(d4), we show four EDS maps for four different elements (silicon, gold, potassium and chloride), within the area depicted in (d). The silicon signal is very uniform. There is no shadowing, which indicates that there is not a considerably thick layer of material (AuNPs) above the surface. The signal for gold is relatively weak and homogeneously distributed across the surface. The signals of potassium and chloride form an halo. This shape is in agreement with the SEM image of the area: there is a higher concentration of AuNPs near the borders of the mapped area and lack of material in the middle. This indicates that a considerable amount of KCl was deposited on the surface of the sample. For our purpose, we want the presence of potassium chloride on the surface of the substrate to be minimal or none, as KCl on the solid state is non-conductive and inhibits charge transport mechanisms. In Figure 3.22(a), we see an SEM image of another region of the same sample. The white vertical strip is an area where there is a larger accumulation of AuNPs, due to the coffee ring effect [82]. The green cross in the image corresponds to the point where we measured an EDS spectrum. We chose a point with lower accumulation of material because it corresponds more closely to the morphology aimed in this work. In Figure 3.22(b), we see the measured EDS spectrum of the point marked on Figure 3.22(a). This spectrum reveals the presence of carbon, silicon, gold, chloride and potassium.

In Figure 3.23(a) and (b), we show SEM images of a sample deposited with AuNPs via spin-coating using the H_2O-based solution of AuNPs (solution *A*). For the deposition, a 120 μL droplet of solution *A* was dropped onto the substrate before each 30-second 800 rpm spin-coating cycle, for a total of 20 cycles. Across the surface, particles are scarcely present. In the particular SEM images of Figure 3.23, there is a large particle (few micrometer size), most possibly a dust particle, which was used to focus the SEM e-beam on the substrate surface. A track is visible due to the particles motion during spin-coating. This particle is isolated and surrounded by a dark stain which is probably a solvent residue. In Figure 3.23(c), we show the measured EDS spectra for this particle. The EDS peaks reveal the presence of calcium, sodium, sulfur and chloride in the constitution of the particle. Oxygen, carbon and silicon are detected as well, although their origin cannot be exactly traced back to the particle since these elements are also common presence on the substrate. No presence of gold was detected in the particle or at the surface. This lack of Au presence is probably due to high centrifugal forces during the spin-coating process and the low wettability of H-terminated silicon when in contact with H_2O. Therefore, we conclude that spin-coating of H_2O-dispersed AuNPs is not an effective method of AuNP deposition as it does not lead to a measurable deposition of AuNPs on the surface.
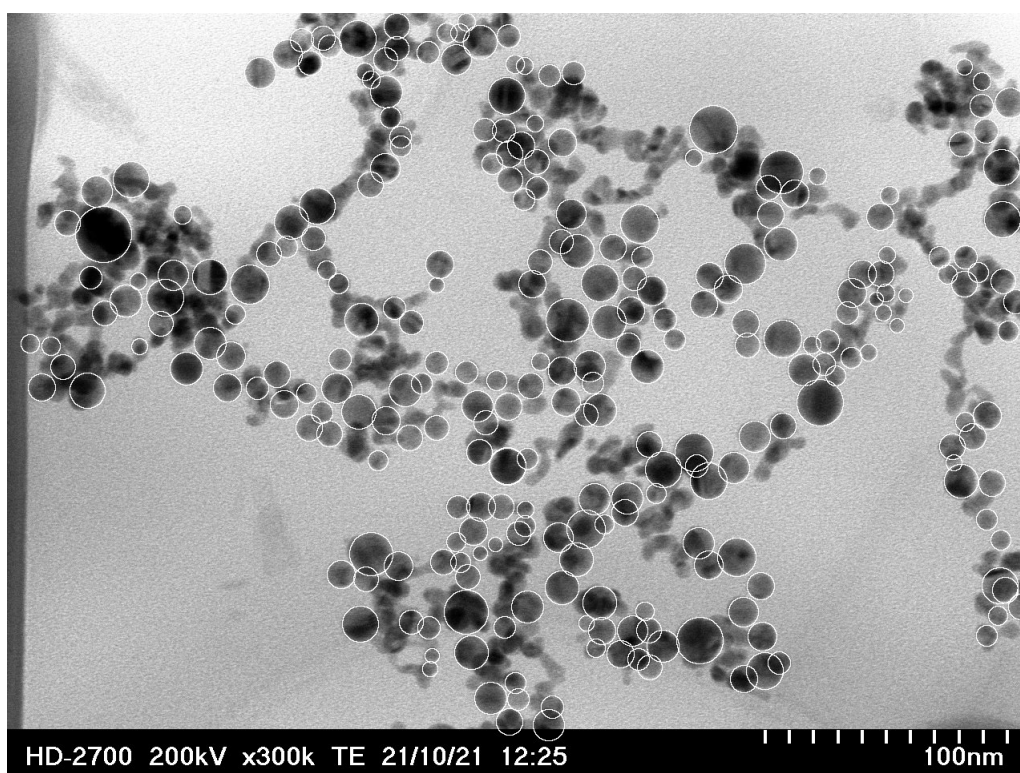
In Figure 3.24, we show SEM images of a silicon substrate after deposition of AuNPs via drop-casting using a solution of AuNPs in THF. Here, a 120 μL droplet of solution *F* was dropped onto the sample surface. The solution was let to rest, until it was completely evaporated over the course of roughly five minutes. There are zones with small clusters AuNPs. In top right of Figure 3.24(a), for example, it is visible the shape of the AuNPs over the silicon background, indicating that the AuNPs are not stacked on top of one another, but instead form

a submonolayer. The clusters of AuNPs irregular shapes and variable sizes and have a disperse and inhomogeneous distribution on the surface. There is also the formation of large clusters, as can be seen in Figure 3.24(b). In order to assess the distribution of Au across the silicon surface, two EDS point acquisitions were carried out. In Figure 3.25(a), we show an SEM image of the AuNP cluster shown in Figure 3.24 and its surrounding area. Points 1 and 2 indicate the location where the two EDS spectra were recorded. These EDS spectra are displayed in Figure 3.25(b). The measured data reveals the presence of carbon, oxygen, silicon, gold and silver. Carbon is detected as it is present in the chemical structure of THF. Silicon belongs to the substrate, amounting to the peak of highest intensity. The presence of oxygen is probably due to the formation of a native oxide on the surface of Si resulting from exposure of the sample to air. The presence of gold confirms that the surface structures are AuNPs. Some nanostructures contain silver, probably due to impurities in the gold target from which the AuNPs were derived during PLAL.

In Figure 3.26, we show SEM images of a silicon substrate after deposition of AuNPs via spin-coating using a dispersion of AuNPs in THF (solution B). The spin-coater was set to the same program as for the deposition with spin-coating using the H_2O-based solution of AuNPs described above. The only difference was before each cycle, a 120 µL droplet of the solution was dropped onto the substrate (instead of 60 µL used for H_2O-based solution). The solvent used for this deposition is THF. As can be seen in Figure 3.26, across the surface, the AuNPs agglomerate themselves in small clusters. The structure of the clusters is elongated, usually resembling a dendrite. The surface coverage is approximately 5%. Bright spherical particles appear dispersed on the substrate. Dark stains are observed in some zones where there is a higher concentration of nanoparticles. It is important to avoid multilayer agglomerates, so that the plasmonic effects are maximized.

Comparing drop-casting against spin-coating using a H_2O-based solution of AuNPs, the first method was better in providing AuNPs to the Si surface. However, drop-casting with H_2O-based solution provided inhomogeneous distributions AuNPs with trace amounts of KCl. Although it is not great, it surpassed the results of spin-coating with H_2O, in which no measurable amount of AuNPs were deposited on the surface. Comparing drop-casting against spin-coating with THF-based solution, the latter method provided better NP distributions. The distribution of NPs from spin-coating was disperse. The main problem is that it lacks surface coverage - only a small quantity of AuNPs is deposited. Although dendritic structures are present, the lack of surface coverage renders the structure inappropriate for (opto-)electronic applications. Overall, THF was the solvent that provided better deposition of AuNPs, due to its effectiveness and consistency in generating thin and homogeneous structures. For it, we adopted THF as solvent of the AuNP solutions for the remainder of the work. Drop-casting and spin-coating, although leading to measurable depositions of AuNPs on silicon surface, appeared lacking in AuNP homogeneity and surface coverage. Thus, we opted to pursue other deposition method besides these two.
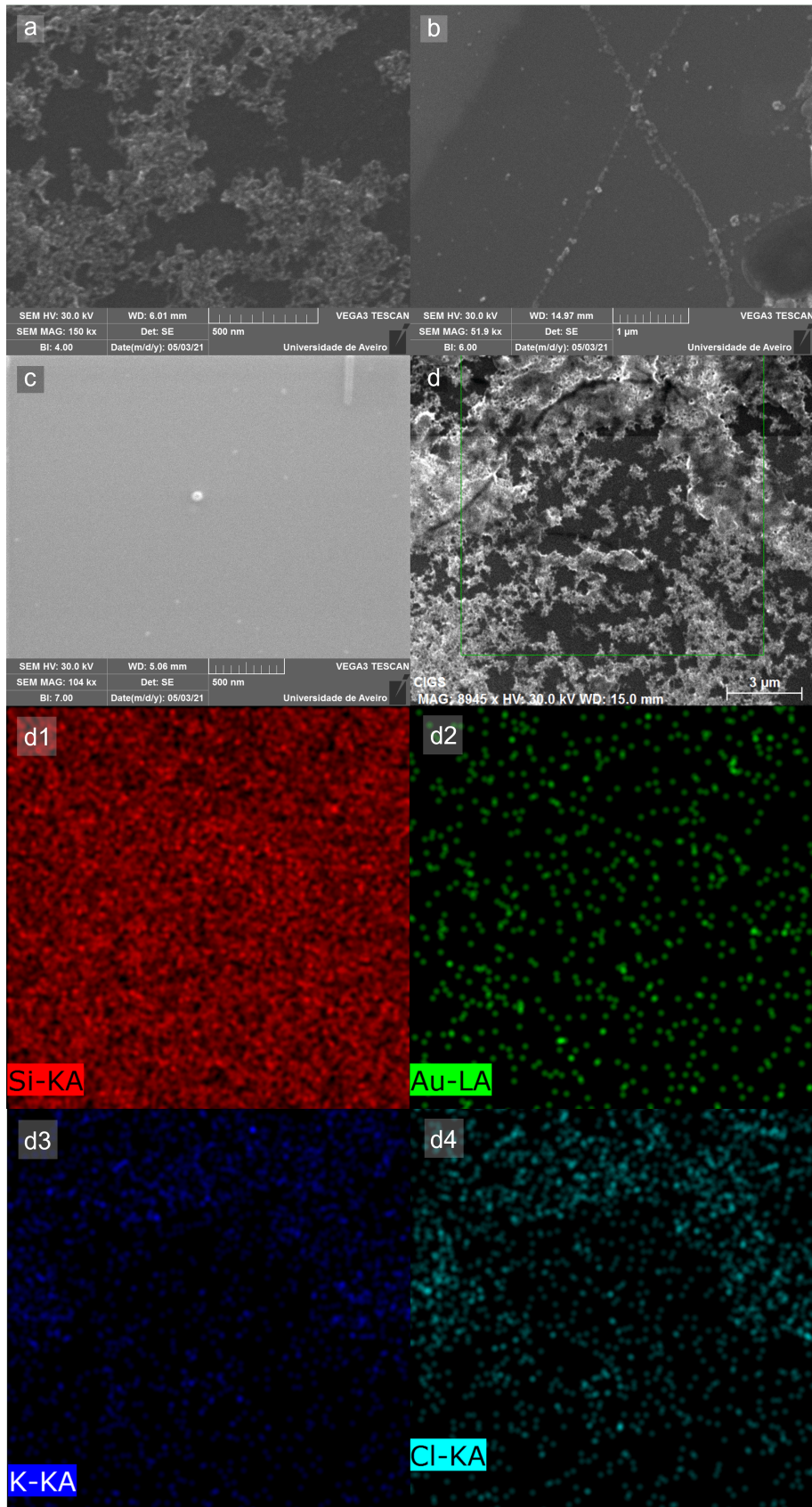
Figure 3.21: (a)-(d) SEM images of silicon substrate after drop-casting of an H_2O-based solution (solution *A*). (d1)-(d4) EDS maps for silicon, gold, potassium and chloride of the sample region reproduced in (d). In (c), there are 2 artifacts that are caused of the SEM electron beam: the bright white dot at the center of the image and the pale gray line on the top right of the image. These should be ignored.
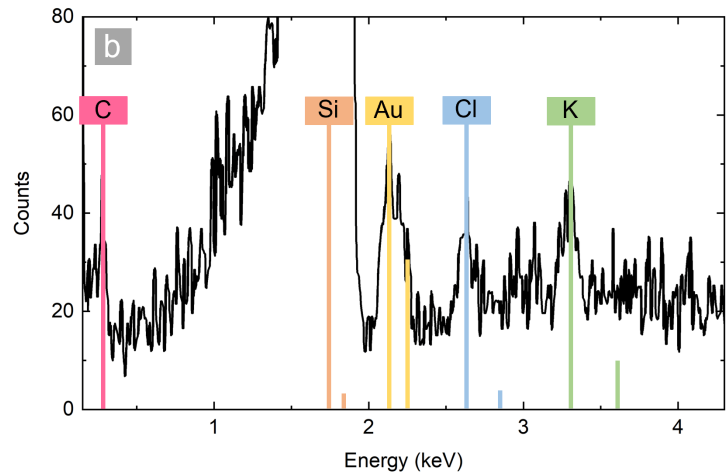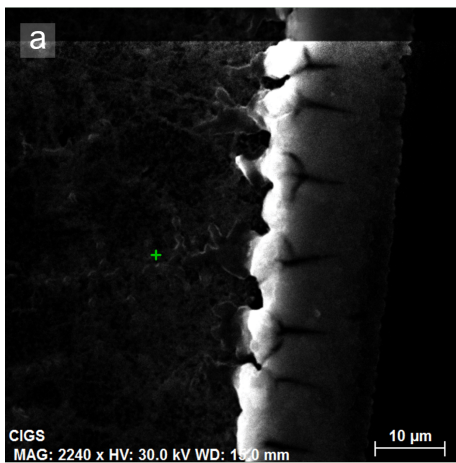
Figure 3.22: (a) SEM image recorded after drop-casting the H_2O-based solution of AuNPs (solution A) (b) EDS spectrum measured on the green cross highlighted in (a).
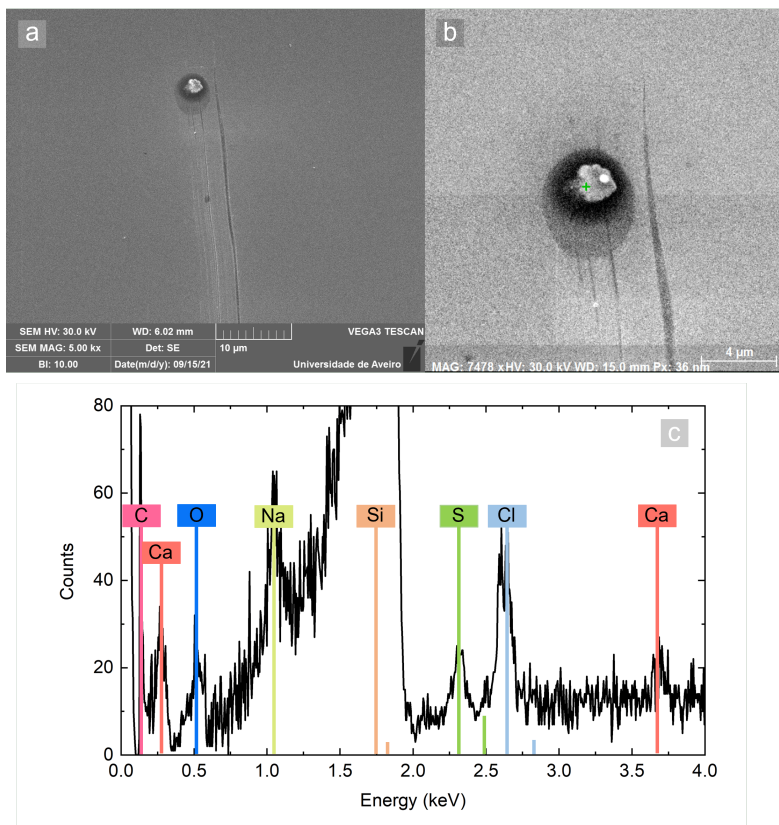
Figure 3.23: (a) SEM image of silicon substrate after spin-coating of the H_2O-based solution of AuNPs (solution A). (b) SEM image of the same zone with higher magnification highlighting the EDS spectrum measurement point with green cross. (c) EDS spectrum measured on the green cross highlighted in (b).
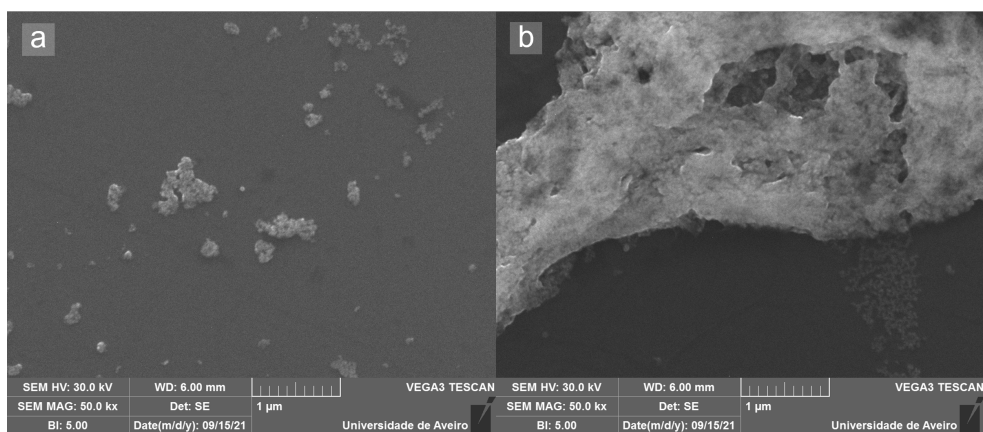
Figure 3.24: (a) and (b) SEM images of silicon substrate after drop-casting of a THF-based solution of AuNPs.
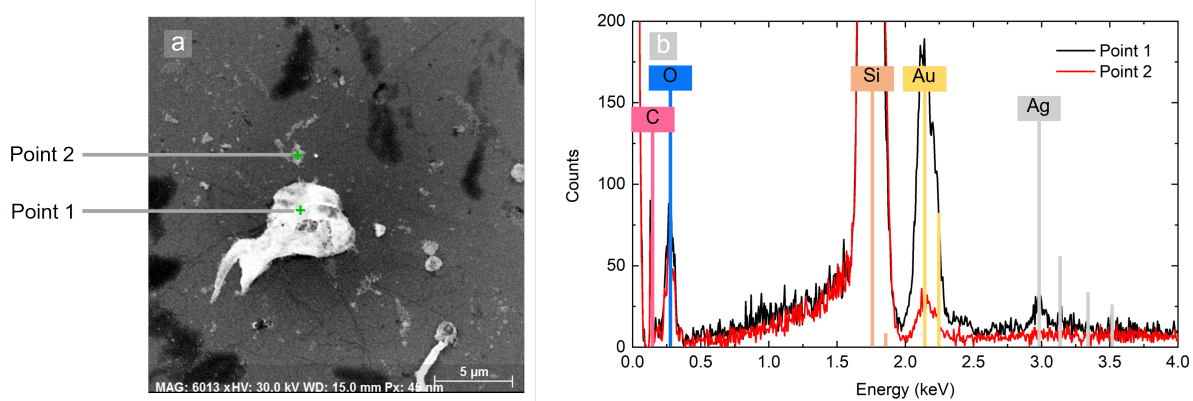
Figure 3.25: (a) SEM image of silicon substrate after drop-casting of a THF-based solution of AuNPs highlighting two EDS spectra measurement points with green crosses.
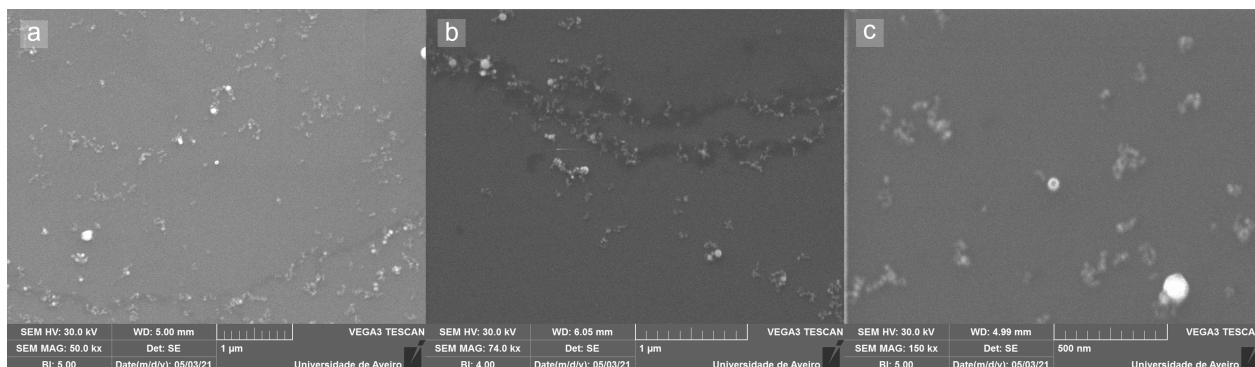
Figure 3.26: (a)-(c) SEM images of silicon substrate after spin-coating of a THF-based solution of AuNPs.

Dip-coating deposition from THF-based solutions
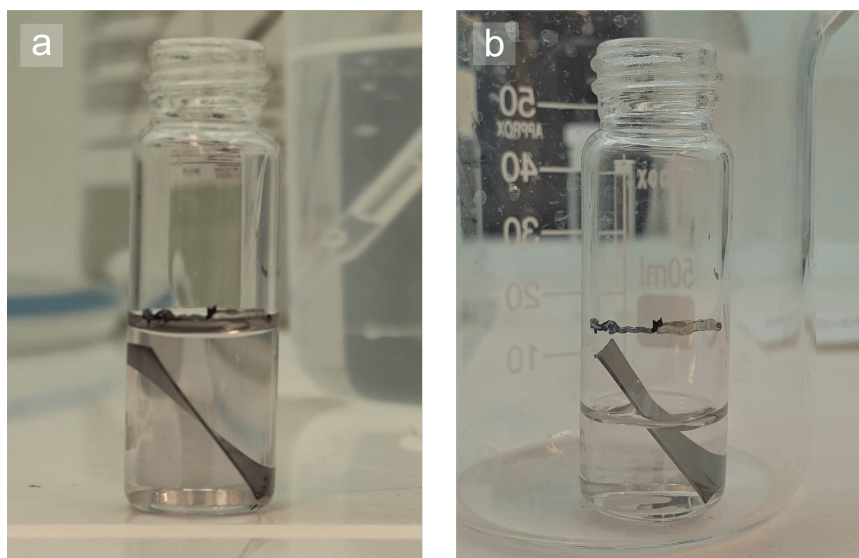
Figure 3.27: Photographs of the dip-coating experimental setup at (a) $t = 0$ h (dip-coating initiated) and (b) $t = 14$ h (dip-coating complete).

The method we opted to study next was dip-coating deposition. In Figure 3.27, we show photographs of a dip-coating experiment. Figure 3.27(a) shows the dip-coating experiment at the time it was initiated and Figure 3.27(b) shows the dip-coating experiment after 14 hours of deposition. We used dip-coating with evaporation, in order to observe the effects that the meniscus traversing the substrate surface had on NP the deposition. The meniscus traversed roughly half the sample. For this dip-coating experiment, solution B (Table 3.1) was used.

In Figures 3.28(a), (c) and (e), we show three images recorded in three different points of the sample surface that was traversed by the meniscus. In Figures 3.28(b), (d) and (f), we show three images of the surface that remained under the solution for the whole deposition time (14 hours). Comparing to the methods previously assessed (spin-coating and drop-casting), AuNP deposition is remarkably more spread out and uniform using the dip-coating method. The surface coverage is also higher than with the aforementioned methods. The size of the Au nanostructures is consistent, ranging from the 100 nm to 500 nm. Ocasionally, AuNPs agglomerate into larger clusters (>1 μm). In these zones, Figure 3.28(d) and (e), the surface coverage diminishes in neighbouring areas. Dark and bright stains appear on the substrate surface traversed by the meniscus.

In Figure 3.29, we show one SEM image of a meniscus traversed region of the same sample as Figure 3.28 and three EDS maps for three different elements on the sample: gold, silicon and carbon. These EDS maps correspond to the area delimited by the green square in Figure 3.29(a). Figure 3.29(b) demonstrates that the particles visible as clustered bright spots in (a) are composed of Au. In Figure 3.29(c), the silicon signal of the substrate is less intense in the region below these AuNP clusters. This weakened signal is due to shadowing by the Au particles. Figure 3.29(d) reveals a trace of carbon in the area corresponding to dark stains in the SEM image. These stains are very likely to be THF residues adsorbed on the silicon surface, since carbon appears in the THF composition.

In order to confirm that gold is not only deposited as large clusters, as seen in Figure 3.29(a), but also spread out along the silicon surface, an EDS point acquisition was carried out. In Figure 3.30(a), we show a SEM image of the analysed zone, with a green cross that corresponds to the point where EDS was measured. We chose a zone without large clustering of AuNPs visible in SEM. In Figure 3.30(b), we show the EDS spectrum of this point. It is detected the presence

33
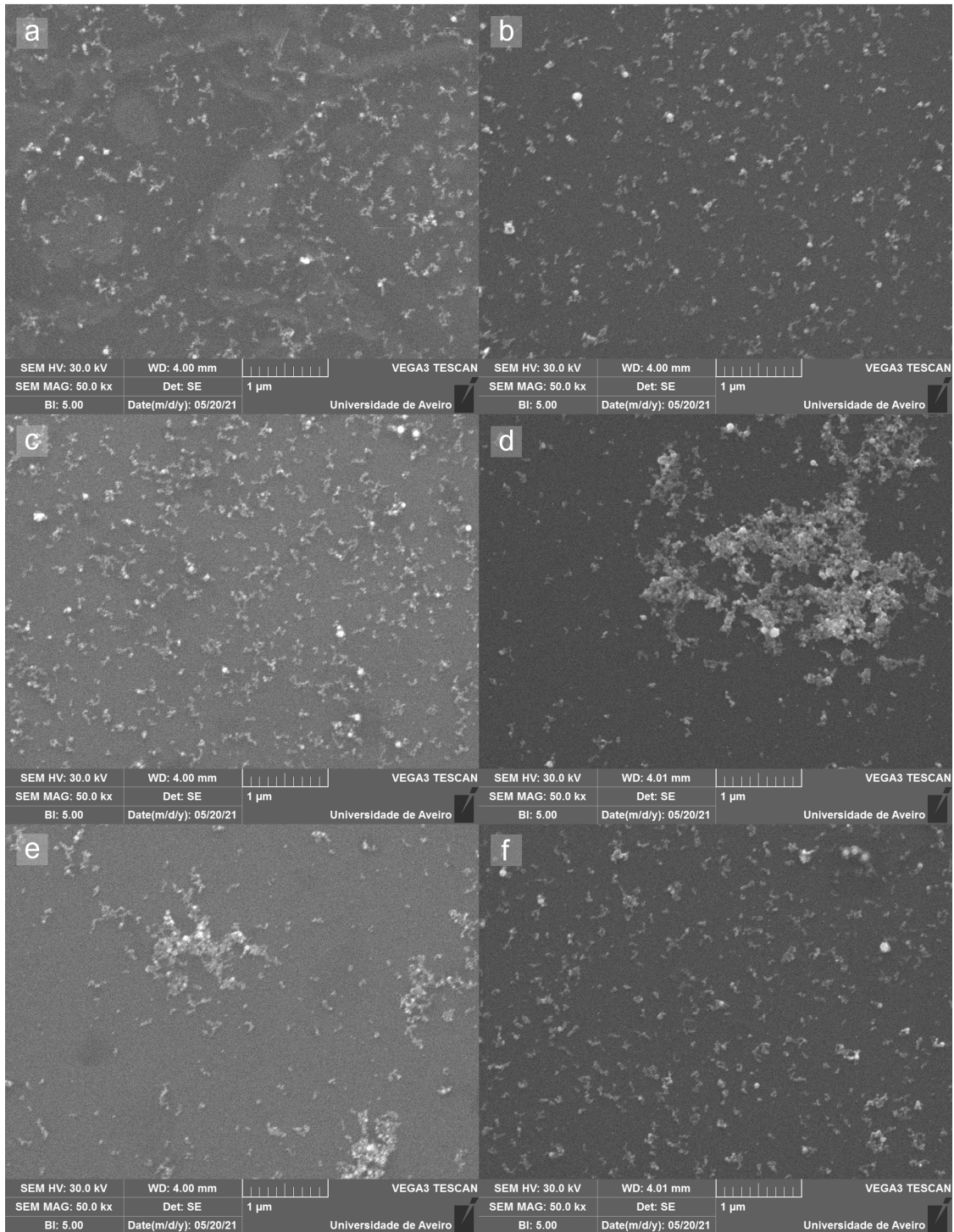
Figure 3.28: SEM images of a silicon substrate after dip-coating deposition using a THF-based solution of AuNPs (solution *B*) with (a),(b),(c) the solvent meniscus traversing the substrate and with (d),(e),(f) the substrate permanently immersed in the AuNP solution.

of gold and carbon. This indicates that the smaller nanostructures on the silicon surface visible in the SEM image of Figure 3.29 are composed of Au.

To attain a better characterization of the Au nanostructures deposited on the surface of Si via dip-coating, we have performed AFM measurements. When performing AFM, it can be unclear whether the observed topology corresponds to the substrate morphology or corresponds to an AuNP structure. Therefore, experiments were devised to tackle this problem by cataloguing the
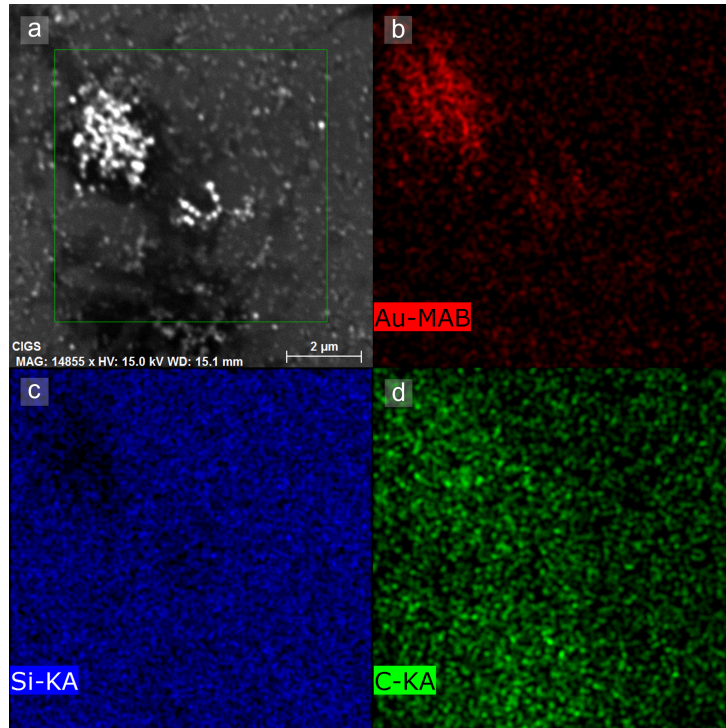
Figure 3.29: (a) SEM image of silicon substrate after dip-coating using THF-based solution B with meniscus traversing the silicon surface, highlighting EDS measurement area with green box. (b)-(d) EDS maps for gold, silicon and carbon of the sample region reproduced in (a).
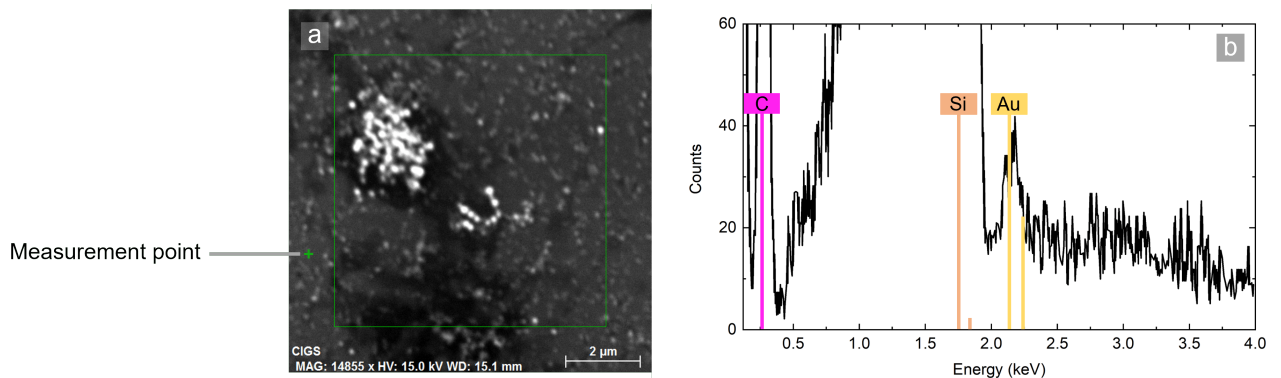
Figure 3.30: (a) SEM image of silicon substrate after dip-coating using THF-based solution, with meniscus traversing the substrate, highlighting EDS spectrum measurement point with green cross. (b) EDS spectrum measured on the green cross highlighted in (a).

morphology of three different substrates which underwent similar treatments as the substrates studied in our work. We will call them samples $S1$, $S2$ and $S3$. Sample $S1$ was subject to our standard silicon substrate cleaning procedure: a 5 minute acetone bath under ultrasonic agitation, followed by an ethanol bath during 5 minutes also under ultrasonic agitation. Sample $S2$ was subject to the same process as sample $S1$, followed by a 5 minute HF-etch. Sample $S3$ was subject to the same process as sample $S2$, followed by a pure THF dip-coating (without AuNPs) for 30 hours. In Figure 3.31(a1), we show an AFM image of the surface of sample $S1$. The roughness across the surface is 0.1 nm. The sample topography, from its lowest trough to its highest peak, is within in a 1 nm range. In Figure 3.31(a2), we can see a height profile plot of the marked red line in Figure 3.31(a1). In Figure 3.31(a3), we show the histogram of the height
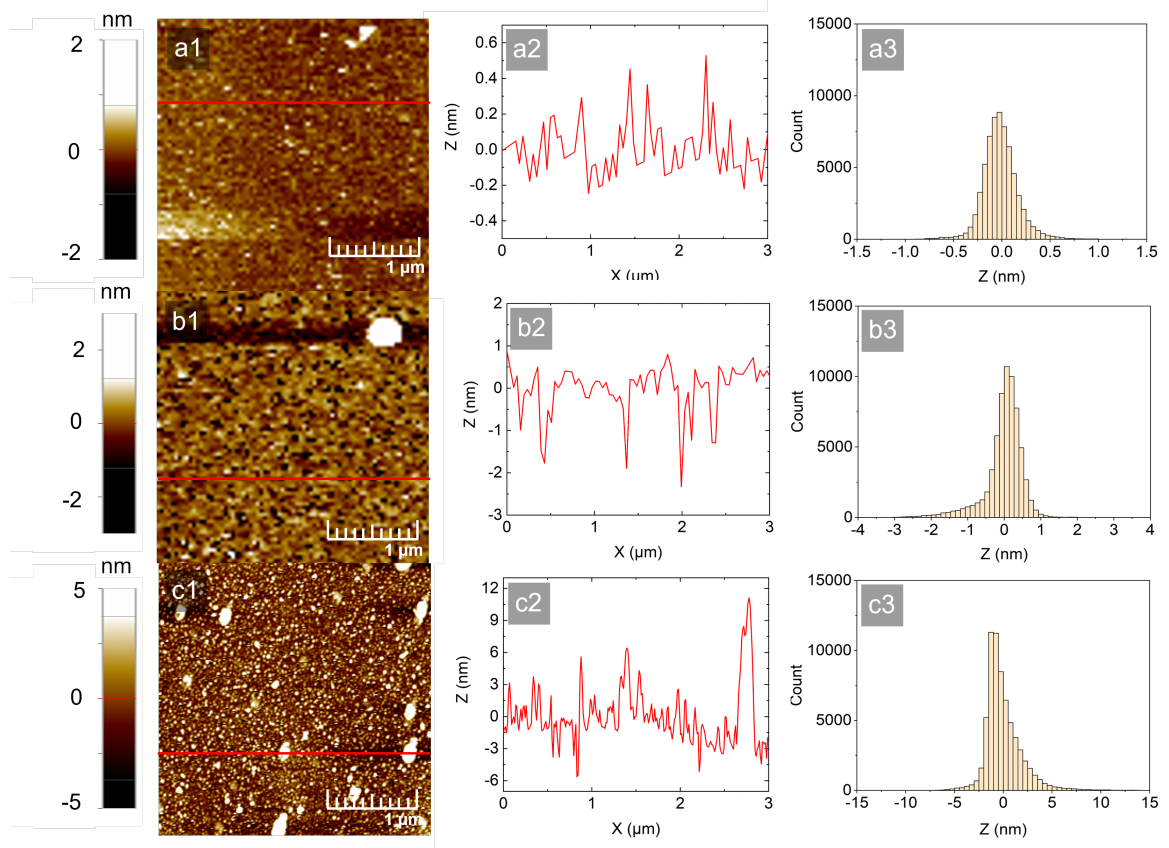
Figure 3.31: AFM images of a silicon substrate after (a1) a 5-minute acetone bath and 5-minute ethanol bath under ultrasonic agitation, (b1) the procedure described in (a1) followed by a 5-minute 5% HF etch and (c1) the procedure described in (b1) followed by a 30-hour dip-coat in THF. (a2)-(c2) Plots of the height profiles of the transverse cuts of the surface highlighted by the red line in (a1)-(c1), respectively. (a3)-(c3) histograms of the height profile distribution of the AFM images in (a1)-(c1), respectively.

profile of the sample. The distribution is not skewed, indicating that the surface of the sample is homogeneous and does not contain nanoparticles. If the sample contained nanoparticles, they would add a contribution to the right side of the height profile histograms, consequently skewing these histograms. In Figure 3.31(b1), we show an AFM image of the surface of sample $S2$. The surface roughness is approximately 0.4 nm. The vertical distance between higher and lower features is increased. Figure 3.31(b2) shows the height profile plot of the marked red line in 3.31(b1). The data demonstrate that an HF etch increases surface roughness. There exist some sharp troughs. The height distribution histogram is skewed to the left, visible in Figure 3.31(b3). This is probably due to the overshoot of the AFM tip after passing over the top right bright particle. In Figure 3.31(c1), we show an AFM image of the surface of sample $S3$. The average surface roughness is approximately 1.3 nm. There are bright circular shaped features distributed evenly across the surface. These features have a wider height amplitude. In Figure 3.31(c2), we can confirm precisely that. The surface of this sample is rougher, as can be seen by average surface roughness value and the spreading of the histogram in Figure 3.31(c3).

In Figures 3.32(a) and (b), we show an SEM image of the surface of the above mentioned sample deposited via dip-coating with a THF-based solution (solution B) and an AFM image of the same sample, respectively. These images have the same scale. Through the AFM measurements, we see that there are two distinct morphology regions. One of these is relatively flat, containing some isolated nanoparticles. Another distinct region of the sample has a higher
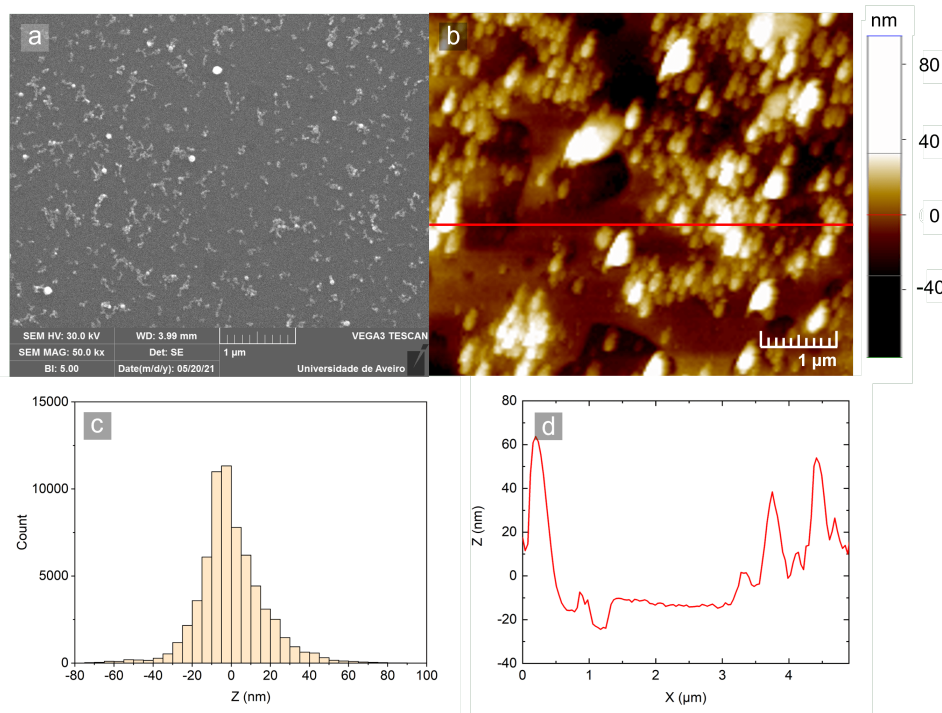
Figure 3.32: (a) SEM image of silicon substrate after dip-coating in the THF-based AuNP solution (solution *B*) with meniscus traversing the substrate. (b) AFM image of the sample. (c) Histogram of the height profile distribution of the AFM image in (b); (d) Height profile of the transverse cut of the surface highlighted by a red line in (b).

---

density of AuNP structures. These structures range from 50 nm up to 1 µm clusters. In Figure 3.32(c), we show the histogram of the height profile of the AFM image. The measured heights range roughly between −40 and 60 nm. The average roughness of the flat regions is roughly 3 nm, while on the nanostructured region it rises to 14 nm. The average roughness of the whole region depicted in Figure 3.32(b) is 12 nm. In Figure 3.32(d), we show the height profile corresponding to the line marked in red in Figure 3.32(b). The measured structures have heights ranging from 10 nm up to 100 nm. Through the scope of AFM, we observe that the topology of the surface is significantly altered after the THF-based deposition of AuNPs. By observing the surface roughness, one is able to differentiate a region which is substrate only (average roughness 3 and relatively small amplitude) from a region of AuNPs deposition (average roughness 10 relatively high amplitude).

From the experiments presented and discussed so far in this Section, it is unclear whether the deposition with the solvent meniscus traversing the substrate or permanent immersion of the substrate produced the better AuNP structures. To answer this question, we carried out further experiments where two substrates are subject to dip-coating, one with the meniscus traversing it during deposition and other permanently immersed in the THF-based dispersion of AuNPs. In the meniscus-traversed sample, the duration of the dip-coating and corresponding meniscus traversing was 22.5 hours. On the permanently immersed sample, the dip-coating spanned 24 hours. For both dip-coating experiments, solution *B* was used.

In Figures 3.33(a) and (c), we show SEM images of the sample prepared by dip-coating with meniscus traversing the substrate, and Figures 3.33(b) and (d) we show SEM images of the sample prepared by dip-coating with permanent immersion. In these experiments, we observed that the meniscus traversing the sample surface promoted the deposition of large AuNP clusters, with a significant fraction of the surface is covered with AuNP structures. On the other hand, dip-coating with permanent immersion originated more uniform, thin and leveled AuNP
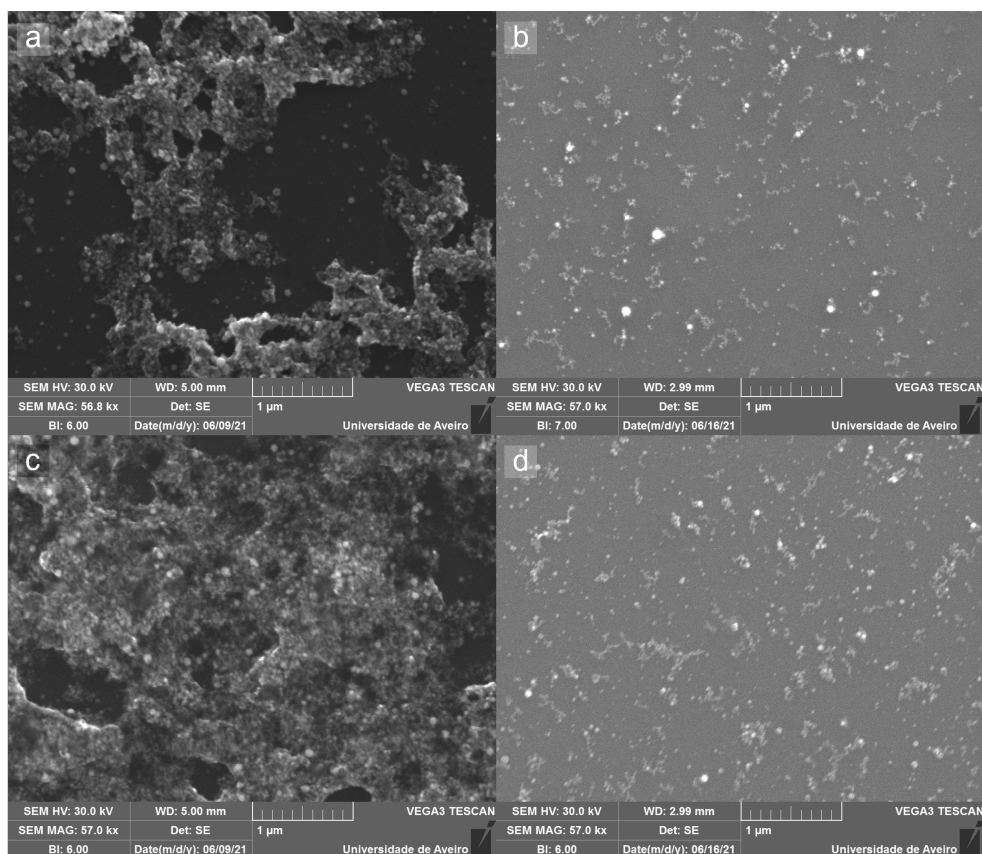
Figure 3.33: SEM images of silicon substrate after (a),(c) 22.5-hour in THF based solution of AuNPs with meniscus traversing the substrate and (b),(d) 24-hour permanently immersed in the same AuNP solution.

structures. Results of Figures 3.28(b) and (f) were largely reproduced in this experiment. Since we aim for the formation of thin sub-monolayer structures of AuNPs, the structure resulting of dip-coating by permanent immersion generates a result closer to what we desire. Therefore, we adopted this procedure for AuNP deposition in all the following experiments.

Influence of deposition time on dip-coating from THF-based solutions

We studied the influence of the deposition time in the distribution of AuNPs on the silicon surface. In Figure 3.34, we show SEM images of three distinct silicon samples deposited with permanent immersion in a THF-based solution (solution B). Figures 3.34[(a),(d)], [(b),(e)] and [(c),(f)] show AuNPs that were deposited in a 6-hour, 24-hour and 4-day dip-coat, respectively. The main influence that deposition time has on the AuNPs distribution is regarding surface coverage. As the deposition time increases, so does the fraction of silicon surface covered by these AuNPs. Surface coverage for the 6-hour, 1-day and 4-day dip-coating with permanent immersion is 4.3%, 9.9% and 14.5% respectively. For the longer dip-coating times, clusters are more uniformly distributed and have consistent dimensions. Dendritic structures are observed for the 24-hour and 4-day dip-coat.

In Figures 3.35(a)-(b) and 3.36(a)-(b), we show SEM images of the surface of the 24-hour dip-coated sample (solution B), side by side with AFM images of the surface of the same sample. In Figures 3.35(b) and 3.36(b), the bright features distributed across the surface are AuNPs. In both SEM and AFM images, it is visible the presence of elongated AuNP structures (AuNPs forming a line) as well as isolated AuNPs. The substrate has small circular structures with heights below 5 nm, which match the morphology of the surface for the THF dip-coating seen
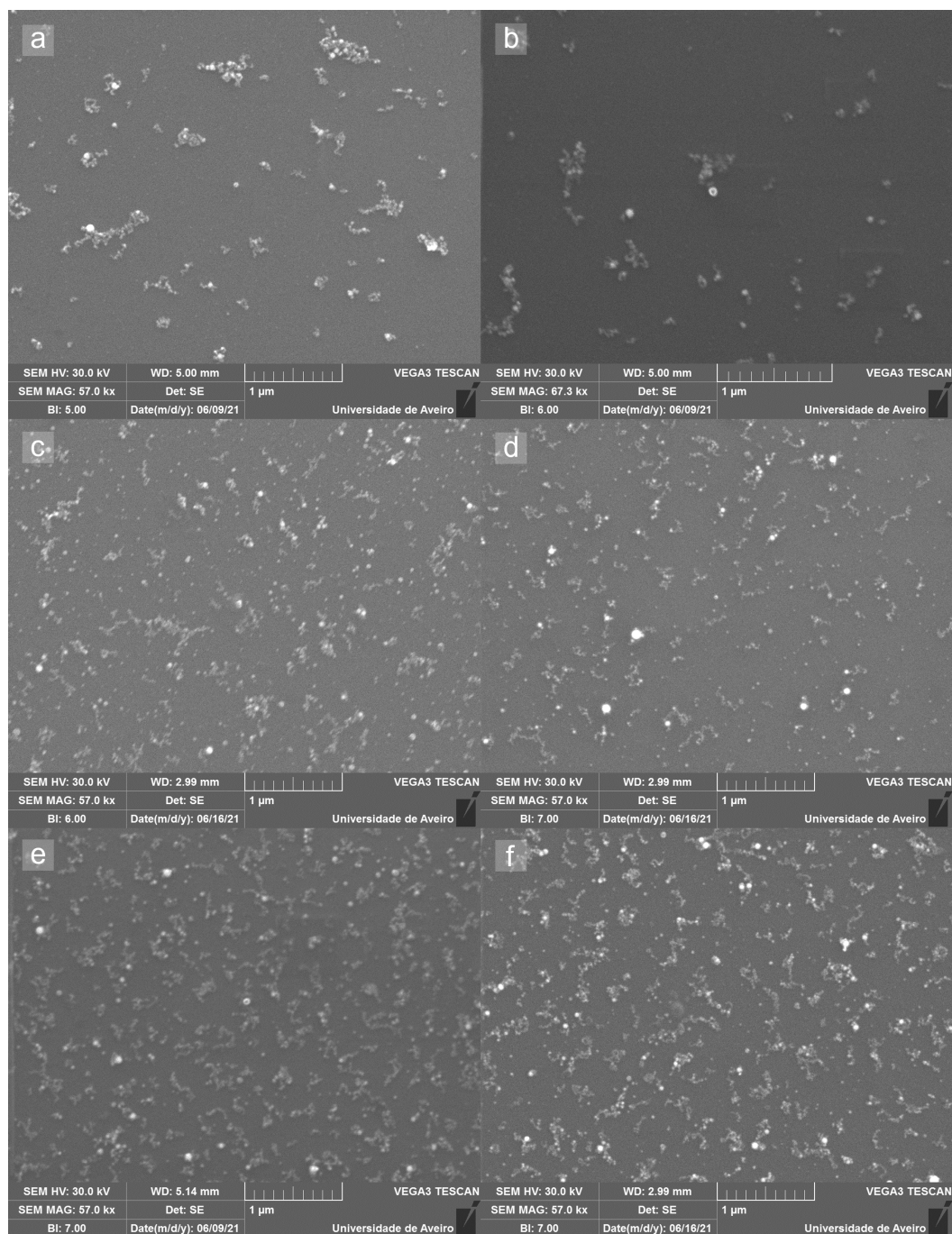
Figure 3.34: SEM images of a silicon substrate after (a) 6-hour, (b) 24-hour and (c) 4-day permanent immersion in a THF-based AuNP solution (solution *B*).

in Figure 3.31(c1). Thus, these small circular structures are probably not AuNPs. In Figures 3.35(c) and 3.36(c), we show the histogram of the height profile of the zone of the sample depicted in Figures 3.35(a) and 3.36(a). The distribution is asymmetrical. The shoulder on the right side of both peaks is indicative of the presence of AuNPs on the surface with sizes in the range of 10-20 nm. In Figures 3.35(d) and 3.36(d), we show the height profile of three transverse cuts of the surface of the sample. It is possible to see a small scale roughness, as was previously seen in Figure 3.31(c2) and large scale features, which corresponds to the AuNPs profiles. According to the SEM and AFM data, AuNPs range from around 10 nm to around 40 nm in diameter. This values are in accordance with the sizes of AuNP structures measured via

Figure 3.35: (a) SEM image of silicon substrate after 24-hour dip-coating with permanent immersion in a THF-based AuNP solution (solution *B*). (b) AFM image of the same sample. (c) Histogram of the height profile distribution of the zone reproduced in (b). (d) Plots of the height profiles of the transverse cuts of the surface highlighted by the red, green and blue lines in (b).

SEM, STEM and absorbance spectra. Despite the dependence of the surface coverage of the substrate on the dip-coating time, practical applications may use multiple parallel dip-coatings to produce a larger AuNP-decorated substrate output.

Influence of AuNP solution synthesis conditions

During AuNPs synthesis via PLAL, there are a number of parameters that can be changed and consequently lead to the production of solutions with different properties. We will focus on two parameters: Q-switch and synthesis duration. We will study their influence on the morphology and distribution of AuNPs. The solutions used for these experiments are solutions *C*, *E* and *F*, which synthesis procedures are described in Section 3.2.1. Three substrates were delicately put inside three small containers. Each container had a substrate that undergone 24-hour dip-coat. To initiate the dip-coating, the three AuNPs solutions were poured into the three distinct containers in a quantity that allowed for full immersion of the substrates. The containers were closed with a lid to avoid solvent evaporation (i.e. permanent immersion of substrates during dip-coating). After 24 hours, the substrates of each of the three containers were removed and stored. Before storing, all substrates were let dry at room temperature, without any post-deposition treatment.

In Figure 3.37, we show SEM images of the surface of the three substrates after a dip-coating of 24 hours, in the case of (a), (b) and (c). Figures 3.37(a), (b) and (c) and were dip-coated with solutions *C*, *E* and *F*, respectively. One parameter tweaked in different AuNP solutions
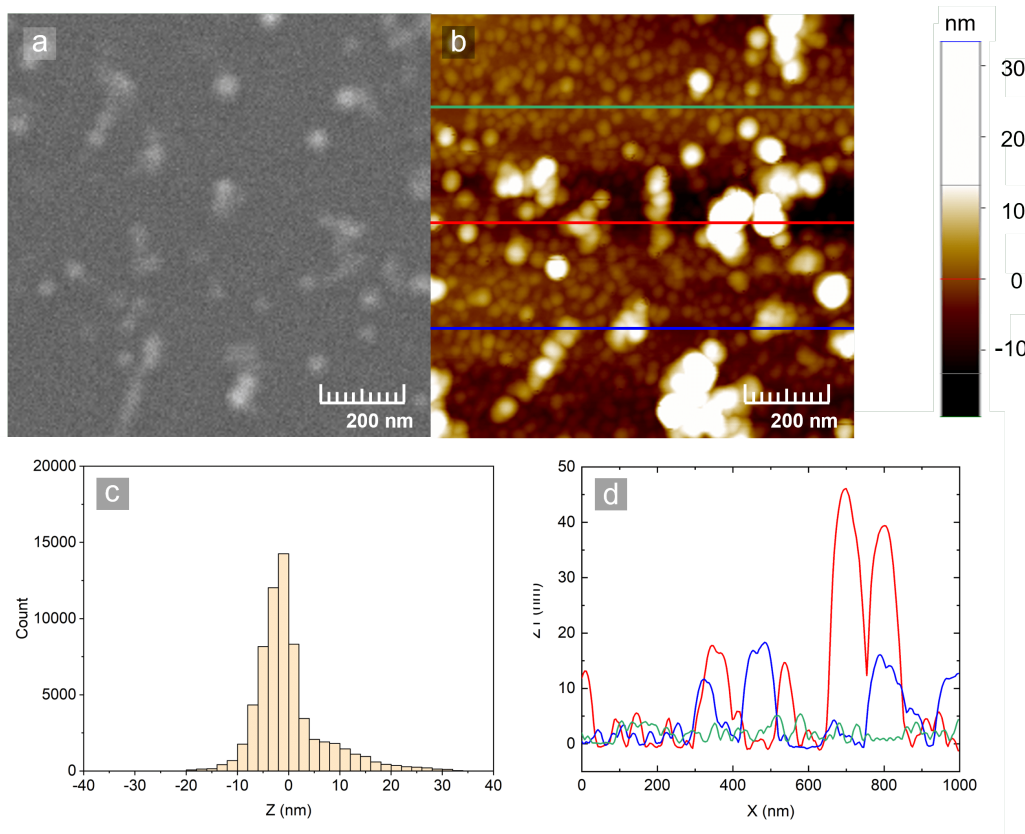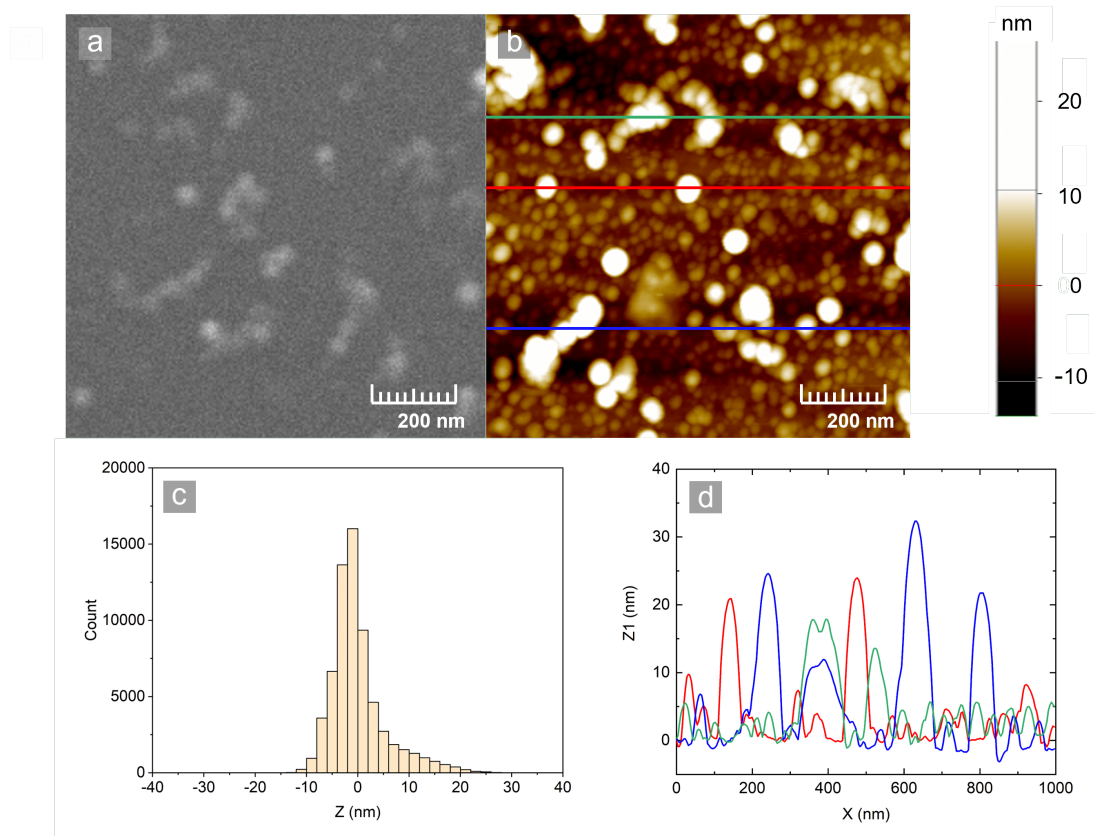
Figure 3.36: (a) SEM image of silicon substrate after 24-hour dip-coating with permanent immersion in a THF-based AuNP solution (solution B). (b) AFM image of the same sample. (c) Histogram of the height profile distribution of the zone reproduced in (b). (d) Plots of the height profiles of the transverse cuts of the surface highlighted by the red, green and blue lines in (b).

was the Q-switch time (solutions C and F). In Figures 3.37(a) and (c), we show the surface of two samples dip-coated for 24 hours in solution C (240 μm Q-switching) and solution E (180 μm Q-switching). In Figure 3.37(a), the AuNPs form clusters with a sub-monolayer structure, some of which are connected by AuNPs pathways, forming larger interconnected clusters with dendritic shape. In Figure 3.37(b), we see larger and denser AuNP formations forming an interconnected mesh. The surface covered by the 240 μm (solution C) and 180 (solution E) μs Q-switched AuNPs is 10% and 31%, respectively. The surface coverage seems to increase with the decrease Q-switch time.

To study the influence of synthesis time of the PLAL AuNP solution on the depositions, we compare samples deposited with solutions E and F; one with synthesis time of 30 min (solution E) and one with synthesis time of 90 min (solution F). All other synthesis parameters were the same and are given in Table 3.1. In Figure 3.37(c), we show the surface of the sample dip-coated (24 hours) in solution F. The AuNPs agglomerate into porous and multi-layered clusters, which at a large scale form an interconnected mesh. The surface covered by the AuNPs in the sample dip-coated in solution F is 38%, which is higher than the 10% surface coverage by the AuNPs on the substrate dip-coated in solution C. The surface coverage by AuNPs seems to increase with the increase in synthesis time, which is expected since the concentration of AuNPs in solution F is expected to be higher than in solution E (due to the longer synthesis time).

41
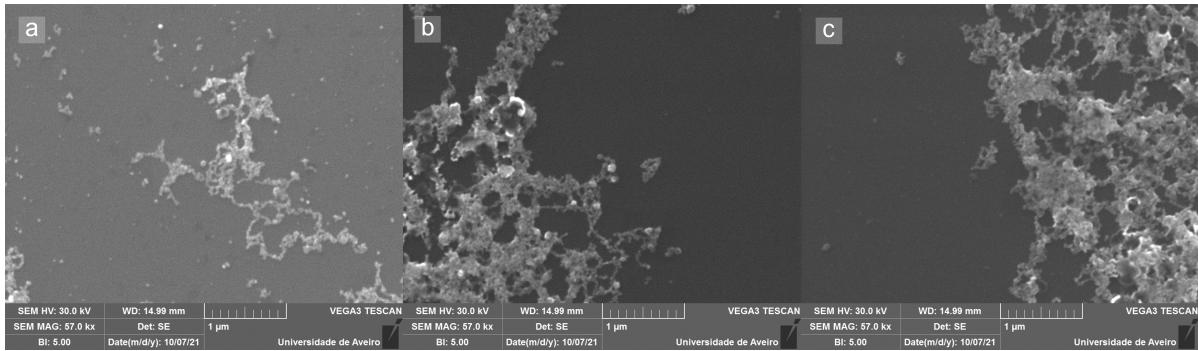
Figure 3.37: SEM images of silicon substrates after dip-coating (permanent immersion for 24 hours) in THF-based AuNP solutions (a) *C*, (b) *E* and (c) *F*.
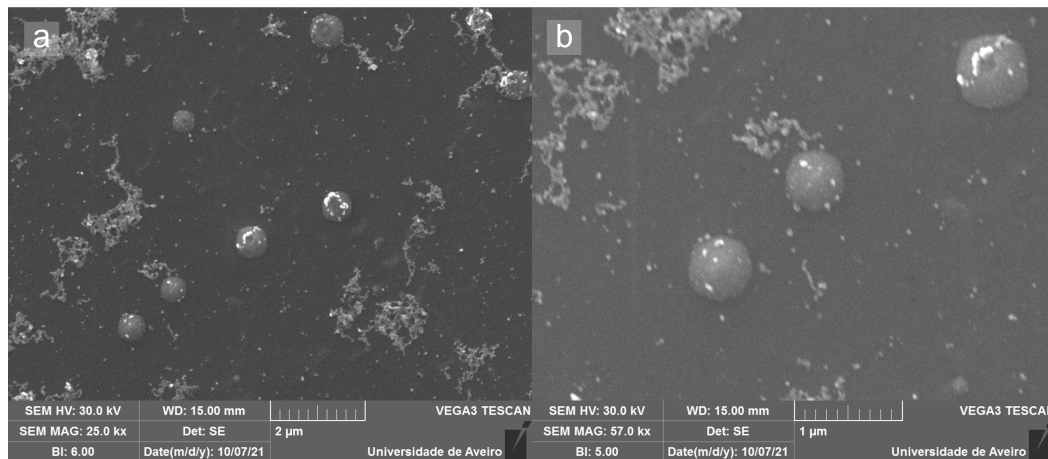
Figure 3.38: (a) and (b) SEM images of a silicon substrate after a 2-hour KOH etching, followed by a 24-hour dip-coating in solution *C*.

3.2.3   Deposition of Au nanostructures onto thinned silicon substrates

Over the course of this work, we studied the thinning of silicon substrates using wet etching with KOH (Section 2.1) and the deposition of AuNP nanostructures onto H-terminated silicon via solution-based methods, focusing on dip-coating of AuNP dispersions in THF (Section 3.2.2). We will now focus on samples that were both thinned and deposited with Au nanostructures. In Figure 3.38, we show SEM images of a substrate that underwent a 2-hours KOH etching, followed a 5 minute acetone bath under ultrasonic agitation and an ethanol bath during 5 minutes also under ultrasonic agitation, before an 5% HF etch for 5 minutes to produce the H-termination of the silicon substrate. After KOH etching, the substrate had a thickness of 235 μm. Then, we dip-coated the sample in solution *C* for a period of 24 hours. As can be seen in Figure 3.38(a), the AuNPs tend to form clusters of dendrite-type shape. These clusters are spread across the surface and somewhat isolated. The surface pyramids visible in the SEM images have AuNPs on their faces. In Figure 3.38(b), we show a SEM image of the same sample with higher magnification. It is visible the presence of isolated non-clustered AuNPs scattered across the surface. In Figure 3.39, we show SEM images of a sample that underwent the same process as described above for the sample shown in Figure 3.38, with the slight alteration of a 5-hour KOH etching (instead of 2-hour). The thickness of the sample was reduced to 90 μm through this process. In this sample, we observe areas with high surface coverage and excess deposition of AuNPs, as in Figure 3.39(a), probably due to surface contaminants as analysed in section 3.1.2 and areas covered with isolated non-clustered AuNPs, as in Figures 3.39(b) and (c). The pyramids are decorated with AuNPs on their surface. The isolated AuNPs in this area
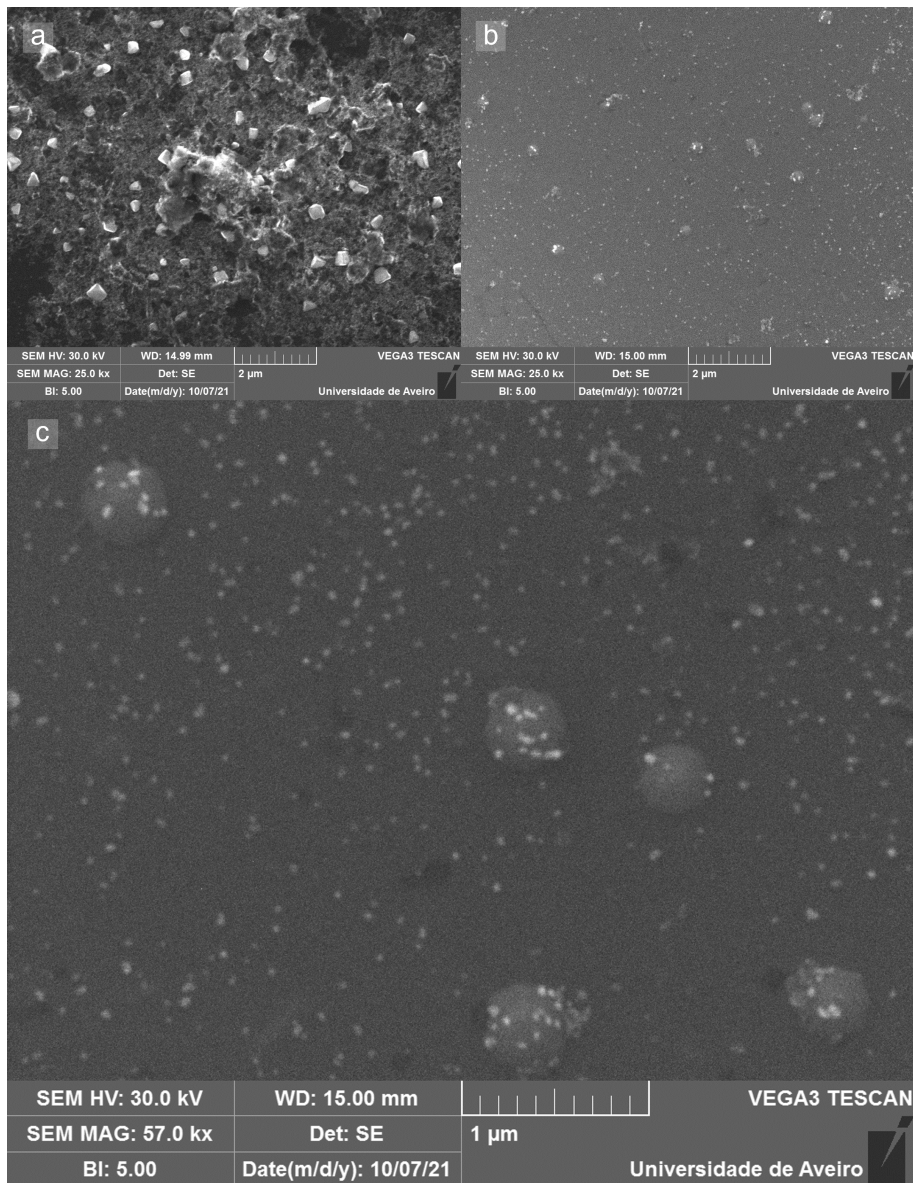
Figure 3.39: [(a),(b),(c)] SEM images of a silicon substrate after a 5-hour KOH etching, followed by a 24-hour dip-coating in solution C.

cover roughly 3% of the surface. All AuNPs are non-clustered and in direct contact with the substrate, which can be significant for charge transport and plasmonic phenomena applications.

Chapter 4

Conclusion and Outlook

In this work, we fabricated and studied H-terminated silicon substrates decorated with plasmonic AuNPs. The goal of this research was to pursue the deposition method that consistently generated AuNP submonolayer structures on an H-terminated silicon surface, due to the increasing relevance this type of plasmonic structures in fields such as photovoltaics and sensing [83, 84].

This work may be divided in three parts. At first, we studied the thinning of silicon via KOH wet chemical etching. This was performed with two different methods, one using an homemade etching cell which predetermined the area of the wafer to be thinned by a KOH solution, and other consisting of a substrate carrier that fully immerses the substrate on an ultrasonically agitated KOH solution. Then, we studied multiple AuNPs deposition methods onto H-terminated silicon substrates. The deposition methods used were drop-casting and spin-coating with both H_2O- and THF-based solutions of AuNPs, and dip-coating with THF-based solution only. Both H_2O- and THF-based AuNPs solutions were fabricated via pulsed laser ablation in liquid (PLAL). Lastly, we used the knowledge gathered from the KOH wet chemical etching of silicon and the solution-based deposition of AuNPs to deposit AuNP nanostructures onto KOH wet chemically etched H-terminated silicon.

It was adopted a homemade process of silicon thinning employing ultrasonic wet chemical etching with 20 wt% KOH with full substrate immersion. This implementation proved to be instrumental to produce up-to sub-50 µm silicon thinned substrates. Concerning the effectiveness of the etching process, it was corroborated that etching under ultrasonic agitation produces flatter thinned silicon, due to the bubble detachment from the surface being promoted and, consequently, the pyramid formation process being dampened. It is imperative to thoroughly clean (with the same procedure to which silicon is subjected before etching) all objects that are to be submerged in the etching operation. This guarantees that the presence of contaminants which may induce pyramid formation is minimized.

It was obtained an experimental etching rate of 0.4 µm/min. Our experimental etching follows very closely the etching rate values reported in the literature using similar conditions. An obstacle we had to overcome was the presence of Fe nanoparticle contaminants after the etching procedure. By cleaning the sample with an alcohol and acetone ultrasonic bath cleaning followed by a 5-minute HF immersion, we demonstrated that it is possible to successfully remove the Fe nanoparticles, while maintaining the underlying silicon morphology intact.

Regarding the AuNPs deposition methods, it was assessed and compared the deposition of AuNP dispersions in both H_2O and THF via the methods of spin-coating, drop-casting and dip-coating (both with and without meniscus traversing the sample). We concluded that spin-coating of H_2O-dispersed AuNPs is not an effective method of AuNP deposition and drop-casting with H_2O-based solution provided inhomogeneous distributions of AuNPs. We also determined that spin-coating with THF lacks surface coverage. Overall, dip-coating provides a remarkably more spread out and uniform AuNP deposition. Concerning the solvents used for the AuNP

dispersions, THF-based AuNP dispersions provided the best depositions when compared to H$_2$O-based AuNP dispersions, due to their effectiveness and consistency in generating thin and homogeneous Au nanostructures. In summary, we concluded that dip-coating with permanent substrate immersion generates thin and levelled structures on the silicon surface, very close to the sub-monolayer structure of AuNPs that we were aiming.

Pertaining the dip-coating process, deposition time increases AuNPs surface coverage and uniformity. For the longer dip-coating times, clusters are more uniformly distributed and have consistent dimensions. Dendritic structures are observed for the 24-hour and 4-day dip-coat. Also, it was observed that longer synthesis time of AuNP solutions leads to larger surface coverage, which is consistent with the higher concentration of AuNPs found in solutions with longer synthesis time. In regard to the influence of the synthesis conditions of the AuNPs dispersions on the dip-coating results, we observed that surface coverage seems increase with the increase in synthesis time and with the decrease Q-switch time.

Finally, we observed that AuNPs deposited via dip-coating on thinned silicon are largely non-clustered and in direct contact with the substrate (i.e., not creating multi-layered structures), a very desirable feature for electronic and optoelectronic applications. They also tend to settle near pyramids on the silicon surface.

Future Work

During this work, we employed wet chemical etching to thin Si substrates. Etch depths of up to 200 μm were attained using this method with ultrasonic agitation. However, upon entering the territory of sub-50 μm of substrate thickness, the violent agitation of the ultrasonic process can damage and wreck these very thin Si substrates. Therefore, alternative methods should be pursued and tested for attaining even thinner Si substrates, for example, abdicating from the ultrasonic agitation at a specific time when the sample is considered fragile. The lack of ultrasonic agitation may lead to an increase of surface roughness, a factor that should be considered and attenuated upon devising a method to achieve very thin sub-50 μm substrates.

Bare AuNPs deposition onto H-terminated silicon substrates using solution-processing methods

During the course of this work, we achieved depositions of Au nanostructures based on bare AuNPs onto H-terminated silicon with large surface coverage by dip-coating pristine H-terminated Si substrates with a THF-based AuNP solution. More studies on applying the solution-based deposition method developed in this thesis to thinned Si substrates can be developed to further improve results. Reflectance measurements of AuNP-decorated substrates can also be carried out to study plasmonic absorbance peaks.

Ultimately, the goal of these investigations is to join a combined effort of delivering plasmonic devices to the industry and consumer levels. Thus, this study can be further supplemented by employing the aforementioned methods (Si wet chemical etching and AuNP PLAL synthesis and dip-coating deposition) in electronic and optoelectronic devices, subsequently studying their efficiency and practicality in real world applications such as plasmonically enhanced photovoltaic cells or high precision sensors.

Bibliography

[1] Troy W Barbee, Stanley Mrowka, and Michael C Hettrick. "Molybdenum-silicon multi-layer mirrors for the extreme ultraviolet". In: *Applied Optics* 24.6 (1985), pp. 883–886.

[2] Daniel Durini. *High performance silicon imaging: fundamentals and applications of cmos and ccd sensors*. Woodhead Publishing, 2019.

[3] *Global Market Outlook For Solar Power 2022-2026*. https://www.solarpowereurope.org/insights/market-outlooks/global-market-outlook-for-solar-power-2022. Accessed: 2022-08-03.

[4] Erik Garnett and Peidong Yang. "Light trapping in silicon nanowire solar cells". In: *Nano letters* 10.3 (2010), pp. 1082–1087.

[5] Yinghuan Kuang et al. "Nanorod solar cell with an ultrathin a-Si: H absorber layer". In: *Applied physics letters* 98.11 (2011), p. 113111.

[6] Amalraj Peter Amalathas and Maan M Alkaisi. "Nanostructures for light trapping in thin film solar cells". In: *Micromachines* 10.9 (2019), p. 619.

[7] Jun Wu. "Absorption enhancement in thin-film solar cells based on periodically chirped structure". In: *Solar Energy* 165 (2018), pp. 85–89.

[8] Wei Liu, Hailing Ma, and Annika Walsh. "Advance in photonic crystal solar cells". In: *Renewable and Sustainable Energy Reviews* 116 (2019), p. 109436.

[9] You Wei et al. "A facile synthesis of segmented silver nanowires and enhancement of the performance of polymer solar cells". In: *Physical Chemistry Chemical Physics* 20.27 (2018), pp. 18837–18843.

[10] R Salimi, AA Sabbagh Alvani, and N Naseri. "Polyol-synthesized plasmonic Ag nanowires for efficient solar energy conversion". In: *2017 IEEE 7th International Conference Nano-materials: Application & Properties (NAP)*. IEEE. 2017, 03NE14–1.

[11] Min Su Kim, Ju Heon Lee, and Moon Kyu Kwak. "Surface texturing methods for solar cell efficiency enhancement". In: *International Journal of Precision Engineering and Manufacturing* 21.7 (2020), pp. 1389–1398.

[12] Harry A Atwater and Albert Polman. "Plasmonics for improved photovoltaic devices". In: *Materials for sustainable energy: a collection of peer-reviewed research and review articles from Nature Publishing Group* (2011), pp. 1–11.

[13] Masoud Shabaninezhad and Guda Ramakrishna. "Theoretical investigation of size, shape, and aspect ratio effect on the LSPR sensitivity of hollow-gold nanoshells". In: *The Journal of Chemical Physics* 150 (Apr. 2019), p. 144116. DOI: 10.1063/1.5090885.

[14] William L Barnes. "Surface plasmonpolariton length scales: a route to sub-wavelength optics". In: *Journal of Optics A: Pure and Applied Optics* 8.4 (Mar. 2006), S87–S93. DOI: 10.1088/1464-4258/8/4/s06. URL: https://doi.org/10.1088/1464-4258/8/4/s06.

[15] Eleonora Petryayeva and Ulrich J. Krull. "Localized surface plasmon resonance: Nanostructures, bioassays and biosensingA review". In: *Analytica Chimica Acta* 706.1 (2011), pp. 8–24. ISSN: 0003-2670. DOI: https://doi.org/10.1016/j.aca.2011.08.020. URL: https://www.sciencedirect.com/science/article/pii/S0003267011011196.

[16] Anran Li et al. "Ultrahigh Enhancement of Electromagnetic Fields by Exciting Localized with Extended Surface Plasmons". In: *The Journal of Physical Chemistry C* 119.33 (2015), pp. 19382–19389. DOI: 10.1021/acs.jpcc.5b05830.

[17] Nina Jiang, Xiaolu Zhuo, and Jianfang Wang. "Active plasmonics: principles, structures, and applications". In: *Chemical reviews* 118.6 (2017), pp. 3054–3099.

[18] Arafeh Bigdeli et al. "Nanoparticle-based optical sensor arrays". In: *Nanoscale* 9.43 (2017), pp. 16546–16563.

[19] Zhengyi Lu et al. "A novel natural surface-enhanced Raman spectroscopy (SERS) substrate based on graphene oxide-Ag nanoparticles-Mytilus coruscus hybrid system". In: *Sensors and Actuators B: Chemical* 261 (2018), pp. 1–10.

[20] Zhenglong Zhang, Daniel Kinzel, and Volker Deckert. "Photo-induced or plasmon-induced reaction: Investigation of the light-induced Azo-coupling of amino groups". In: *The Journal of Physical Chemistry C* 120.37 (2016), pp. 20978–20983.

[21] Luchao Du et al. "Plasmon induced charge transfer mechanism in gold-TiO2 nanoparticle systems: The size effect of gold nanoparticle". In: *Journal of Applied Physics* 128.21 (2020), p. 213104.

[22] Alberto Alvarez-Fernandez et al. "Block copolymer directed metamaterials and metasurfaces for novel optical devices". In: *Advanced Optical Materials* 9.16 (2021), p. 2100175.

[23] Arati Mehere and Nandu B Chaure. "Precisely controlled shape and size of gold nanostructures by seed-mediated reduction reaction method". In: *Applied Physics A* 126.8 (2020), pp. 1–14.

[24] Cristiano Matricardi et al. "Gold nanoparticle plasmonic superlattices as surface-enhanced Raman spectroscopy substrates". In: *ACS nano* 12.8 (2018), pp. 8531–8539.

[25] Gizem Birant et al. "Plasmonic light-management interfaces by polyol-synthesized silver nanoparticles for industrial scale silicon solar cells". In: *ACS Applied Nano Materials* 3.12 (2020), pp. 12231–12239.

[26] OO Havryliuk et al. "Plasmonic enhancement of light to improve the parameters of solar cells". In: *Applied Nanoscience* 10.12 (2020), pp. 4759–4766.

[27] Supachai Sompech et al. "Theoretical calculation of optical absorption property of Cu@ Ag core–shell composite nanoparticle". In: *Materials Research Express* 6.2 (2018), p. 026201.

[28] Claudia de Melo et al. "Tunable localized surface plasmon resonance and broadband visible photoresponse of Cu nanoparticles/ZnO surfaces". In: *ACS applied materials & interfaces* 10.47 (2018), pp. 40958–40965.

[29] Adam Ginsburg et al. "Solid state ITO| Au-NPs| TiO2 plasmonic based solar cells". In: *Solar Energy Materials and Solar Cells* 179 (2018), pp. 254–259.

[30] Vivek Garg et al. "Localized surface plasmon resonance on Au nanoparticles: tuning and exploitation for performance enhancement in ultrathin photovoltaics". In: *RSC advances* 6.31 (2016), pp. 26216–26226.

[31] Keisuke Nakamura et al. "Properties of plasmon-induced photoelectric conversion on a TiO2/NiO p–n junction with Au nanoparticles". In: *The journal of physical chemistry letters* 7.6 (2016), pp. 1004–1009.

[32] Qi Xu et al. "Enhanced broadband light trapping in c-Si solar cells using nanosphere-embedded metallic grating structure". In: *IEEE Journal of Photovoltaics* 6.1 (2015), pp. 61–67.

[33] Michael Riordan, Lillian Hoddeson, and Conyers Herring. "The Invention of the Transistor". In: *More Things in Heaven and Earth: A Celebration of Physics at the Millennium*. Ed. by Benjamin Bederson. New York, NY: Springer New York, 1999, pp. 563–578. ISBN: 978-1-4612-1512-7. DOI: 10.1007/978-1-4612-1512-7_37. URL: https://doi.org/10.1007/978-1-4612-1512-7_37.

[34] Hidenori Mizuno et al. "Transfer-printed silver nanodisks for plasmonic light trapping in hydrogenated microcrystalline silicon solar cells". In: *Applied Physics Express* 7.11 (2014), p. 112302.

[35] Sui Mao et al. "Morphological and optical evolution of metallic oxide/Au nanoparticle hybrid thin film: High absorption and reflectance by plasmonic enhancement". In: *Applied Surface Science* 495 (2019), p. 143575.

[36] Zijie Yan and Douglas B Chrisey. "Pulsed laser ablation in liquid for micro-/nanostructure generation". In: *Journal of Photochemistry and Photobiology C: Photochemistry Reviews* 13.3 (2012), pp. 204–223.

[37] Mònica Fernández-Arias et al. "Synthesis and deposition of Ag nanoparticles by combining laser ablation and electrophoretic deposition techniques". In: *Coatings* 9.9 (2019), p. 571.

[38] Björn Hoffmann et al. "Fabrication and characterization of plasmonic nanocone antennas for strong spontaneous emission enhancement". In: *Nanotechnology* 26.40 (2015), p. 404001.

[39] Fumihiro Inoue et al. "Influence of Si wafer thinning processes on (sub)surface defects". In: *Applied Surface Science* 404 (2017), pp. 82–87. ISSN: 0169-4332. DOI: https://doi.org/10.1016/j.apsusc.2017.01.259. URL: https://www.sciencedirect.com/science/article/pii/S0169433217302829.

[40] E Estragnat et al. "Experimental investigation on mechanisms of silicon chemical mechanical polishing". In: *Journal of electronic materials* 33.4 (2004), pp. 334–339.

[41] *Wafer Thinning: Techniques for Ultra-thin Wafers*. https://sst.semiconductor-digest.com/2003/03/wafer-thinning-techniques-for-ultra-thin-wafers/. Accessed: 2022-06-06.

[42] Xixi Wang et al. "Heterojunction hybrid solar cells by formation of conformal contacts between PEDOT: PSS and periodic silicon nanopyramid arrays". In: *Small* 14.15 (2018), p. 1704493.

[43] Kazuya Tsujino and Michio Matsumura. "Helical nanoholes bored in silicon by wet chemical etching using platinum nanoparticles as catalyst". In: *Electrochemical and Solid-State Letters* 8.12 (2005), p. C193.

[44] Huseyin Ekinci, Bo Cui, and Dmitry Pushin. "Fabrication of sub-micron trenches with surfactant-added KOH". In: *2020 IEEE 20th International Conference on Nanotechnology (IEEE-NANO)*. IEEE. 2020, pp. 172–175.

[45] H Angermann et al. "Wet-chemical passivation and characterization of silicon interfaces for solar cell applications". In: *Solar energy materials and solar cells* 83.4 (2004), pp. 331–346.

[46] Zhe Ma et al. "Heavily boron-doped silicon layer for the fabrication of nanoscale thermoelectric devices". In: *Nanomaterials* 8.2 (2018), p. 77.

[47] Jing Chen et al. "Study of anisotropic etching of (1 0 0) Si with ultrasonic agitation". In: *Sensors and Actuators A: Physical* 96.2-3 (2002), pp. 152–156.

[48] Chun-Chi Lin et al. "Tetramethylammonium hydroxide poisoning". In: *Clinical toxicology* 48.3 (2010), pp. 213–217.

[49] E Herr and H Baltes. "KOH etching of high-index crystal planes in silicon". In: *Sensors and Actuators A: Physical* 31.1-3 (1992), pp. 283–287.

[50] Kazuo Sato et al. "Characterization of orientation-dependent etching properties of single-crystal silicon: effects of KOH concentration". In: *Sensors and Actuators A: Physical* 64.1 (1998), pp. 87–93.

[51] H Seidel et al. "Anisotropic etching of crystalline silicon in alkaline solutions: I. Orientation dependence and behavior of passivation layers". In: *Journal of the electrochemical society* 137.11 (1990), p. 3612.

[52] Don L Kendall. "Vertical etching of silicon at very high aspect ratios". In: *Annual Review of Materials Science* 9.1 (1979), pp. 373–403.

[53] Minkyu Ju et al. "The effect of small pyramid texturing on the enhanced passivation and efficiency of single c-Si solar cells". In: *RSC advances* 6.55 (2016), pp. 49831–49838.

[54] MA Gosálvez and RM Nieminen. "Surface morphology during anisotropic wet chemical etching of crystalline silicon". In: *New Journal of Physics* 5.1 (2003), p. 100.

[55] *Fabrication of Microfluidic devices using Etching.* http://www.aesociety.org/areas/microfluidic_chips/etching.php. Accessed: 2021-10-26.

[56] H Schröder, E Obermeier, and A Steckenborn. "Micropyramidal hillocks on KOH etched {100} silicon surfaces: formation, prevention and removal". In: *Journal of Micromechanics and Microengineering* 9.2 (1999), p. 139.

[57] SA Campbell et al. "Inhibition of pyramid formation in the etching of Si p (100) in aqueous potassium hydroxide-isopropanol". In: *Journal of Micromechanics and Microengineering* 5.3 (1995), p. 209.

[58] H Tanaka et al. "Effects of small amount of impurities on etching of silicon in aqueous potassium hydroxide solutions". In: *Sensors and Actuators A: Physical* 82.1-3 (2000), pp. 270–273.

[59] PMMC Bressers et al. "Surface morphology of p-type (100) silicon etched in aqueous alkaline solution". In: *Journal of the Electrochemical Society* 143.5 (1996), p. 1744.

[60] Yibo Zeng et al. "A new processing technique for fabrication of ultra-thin wafer." In: *International Journal of Advanced Manufacturing Technology* 100 (2019).

[61] *FTIR spectroscopy.* https://photobioschool.ru/en/methods-en/ftir-spectroscopy/. Accessed: 2021-10-26.

[62] *VERTEX 80/80v FT-IR Spectrometers.* https://www.bruker.com/en/products-and-solutions/infrared-and-raman/ft-ir-research-spectrometers/vertex-research-ft-ir-spectrometer/vertex-80-80v-ft-ir-spectrometer.html. Accessed: 2022-18-10.

[63] Ali Akbar Ashkarran and Alireza Bayat. "Surface plasmon resonance of metal nanostructures as a complementary technique for microscopic size measurement". In: *International Nano Letters* 3.1 (2013), pp. 1–10.

[64] Wolfgang Haiss et al. "Determination of size and concentration of gold nanoparticles from UV- Vis spectra". In: *Analytical chemistry* 79.11 (2007), pp. 4215–4221.

[65] Nikolai G Khlebtsov. "Determination of size and concentration of gold nanoparticles from extinction spectra". In: *Analytical chemistry* 80.17 (2008), pp. 6620–6625.

[66] *UV Talk Letter.* https://www.shimadzu.eu/sites/shimadzu.seg/files/uvtalklettervol16.pdf. Accessed: 2022-01-27.

[67] JitKang Lim et al. "Characterization of magnetic nanoparticle by dynamic light scattering". In: *Nanoscale research letters* 8.1 (2013), pp. 1–14.

[68] *Zetasizer Nano ZS*. `https://www.malvernpanalytical.com/en/support/product-support/zetasizer-range/zetasizer-nano-range/zetasizer-nano-zs`. Accessed: 2022-18-10.

[69] *SEM vs TEM*. `https://www.technologynetworks.com/analysis/articles/sem-vs-tem-331262`. Accessed: 2022-10-07.

[70] *Tescan VEGA 3*. `https://www.tescan.com/product/sem-for-materials-science-tescan-vega/`. Accessed: 2022-18-10.

[71] *HD-2700 Cs-Corrected FE-STEM*. `https://www.hitachi-hightech.com/file/us/pdf/library/literature/Hitachi-HD-2700FE-STEM-HTD-E171_0.pdf`. Accessed: 2022-18-10.

[72] *How does atomic force microscopy work?* `https://www.quora.com/How-does-atomic-force-microscopy-work`. Accessed: 2021-10-26.

[73] *XEI Manual - ASU Core Facilities*. `https://cores.research.asu.edu/sites/default/files/2020-08/XEIManual_1_8_0_0.pdf`. Accessed: 2022-08-04.

[74] MH Yun, VA Burrows, and MN Kozicki. "Analysis of KOH etching of (100) silicon on insulator for the fabrication of nanoscale tips". In: *Journal of Vacuum Science & Technology B: Microelectronics and Nanometer Structures Processing, Measurement, and Phenomena* 16.5 (1998), pp. 2844–2848.

[75] HH Li. "Refractive index of silicon and germanium and its wavelength and temperature derivatives". In: *Journal of Physical and Chemical Reference Data* 9.3 (1980), pp. 561–658.

[76] MH Yun, VA Burrows, and MN Kozicki. "Analysis of KOH etching of (100) silicon on insulator for the fabrication of nanoscale tips". In: *Journal of Vacuum Science & Technology B: Microelectronics and Nanometer Structures Processing, Measurement, and Phenomena* 16.5 (1998), pp. 2844–2848.

[77] Kirt R Williams, Kishan Gupta, and Matthew Wasilik. "Etch rates for micromachining processing-Part II". In: *Journal of microelectromechanical systems* 12.6 (2003), pp. 761–778.

[78] AI Frenkel et al. "Size-controlled synthesis and characterization of thiol-stabilized gold nanoparticles". In: *The Journal of chemical physics* 123.18 (2005), p. 184701.

[79] Jingfang Zhou et al. "Functionalized gold nanoparticles: synthesis, structure and colloid stability". In: *Journal of colloid and interface science* 331.2 (2009), pp. 251–262.

[80] Layal L Rouhana, Jad A Jaber, and Joseph B Schlenoff. "Aggregation-resistant water-soluble gold nanoparticles". In: *Langmuir* 23.26 (2007), pp. 12799–12801.

[81] Young-Jin Yoon et al. "Water-Redispersible and Highly Stable Gold Nanoparticles Permanently Capped by Charge-Controllable Surfactants for Potential Medical Applications". In: *ACS Applied Nano Materials* 2.12 (2019), pp. 7924–7932.

[82] Archana Kaliyaraj Selva Kumar et al. "A mini-review: How reliable is the drop casting technique?" In: *Electrochemistry Communications* 121 (2020), p. 106867.

[83] Ming-Chung Chen et al. "Self-assembled monolayer immobilized gold nanoparticles for plasmonic effects in small molecule organic photovoltaic". In: *ACS Applied Materials & Interfaces* 5.3 (2013), pp. 511–517.

[84] Cheng-Dah Chen et al. "Sensing capability of the localized surface plasmon resonance of gold nanorods". In: *Biosensors and Bioelectronics* 22.6 (2007), pp. 926–932.